DISEASES AND DISORDERS

Adrenomedullin has a pivotal role in trophoblast differentiation: A promising nanotechnology-based therapeutic target for early-onset preeclampsia

Qingqing Zhang[1,2]†, Cheuk-Lun Lee[1,2]†, Tingyu Yang[3,4]†, Jianlin Li[1], Qunxiong Zeng[2], Xiaofeng Liu[2], Zhongzhen Liu[3,5], Degong Ruan[6], Zhuoxuan Li[6], Anita S. Y. Kan[7], Ka-Wang Cheung[1], Annisa S. L. Mak[8], Vivian W. Y. Ng[7], Huashan Zhao[9], Xiujun Fan[9], Yong-Gang Duan[2], Liuying Zhong[10], Min Chen[11], Meirong Du[12], Raymond H. W. Li[1,2], Pengtao Liu[6], Ernest H. Y. Ng[1,2], William S. B. Yeung[1,2], Ya Gao[3,5]*, Yuanqing Yao[2]*, Philip C. N. Chiu[1,2]*

Early-onset preeclampsia (EOPE) is a severe pregnancy complication associated with defective trophoblast differentiation and functions at implantation, but manifestation of its phenotypes is in late pregnancy. There is no reliable method for early prediction and treatment of EOPE. Adrenomedullin (ADM) is an abundant placental peptide in early pregnancy. Integrated single-cell sequencing and spatial transcriptomics confirm a high ADM expression in the human villous cytotrophoblast and syncytiotrophoblast. The levels of ADM in chorionic villi and serum were lower in first-trimester pregnant women who later developed EOPE than those with normotensive pregnancy. ADM stimulates differentiation of trophoblast stem cells and trophoblast organoids in vitro. In pregnant mice, placenta-specific ADM suppression led to EOPE-like phenotypes. The EOPE-like phenotypes in a mouse PE model were reduced by a placenta-specific nanoparticle-based forced expression of ADM. Our study reveals the roles of trophoblastic ADM in placental development, EOPE pathogenesis, and its potential clinical uses.

INTRODUCTION

Preeclampsia (PE) is a serious pregnancy complication affecting 2 to 5% of pregnancies worldwide, leading to >60,000 maternal and >500,000 infant deaths annually. It is associated with a high incidence of fetal growth restriction (FGR) and short- and long-term maternal and perinatal complications. Therefore, PE is a substantial burden on global health care systems (*1*).

PE is a placenta-related disease. Structurally, a chorionic villous is the functional unit of the placenta. Each villous consists of a stromal core, a layer of villous cytotrophoblast (VCT) surrounding the stromal core, and a layer of multinucleated syncytiotrophoblasts (SCTs) on the outside of the VCT forming the outermost surface of the villous tree (*2*). The stromal core contains Hofbauer cells, chorionic villous mesenchymal stem/stromal cells, and endothelial cells of the embryo (*2*). During human placentation, the proliferative stem cell–like VCT fuses to form the SCT responsible for hormone production and maintenance of homeostasis in pregnancy, or they can penetrate the SCT in the anchoring villi and differentiate into extravillous trophoblast (EVT) that invades the decidua and spiral arteries in the first 12 weeks of pregnancy (*3*).

PE is classified as early- and late-onset types: Early-onset preeclampsia (EOPE) occurs before 34 weeks of gestation and is the most severe clinical variant of the disease. It is associated with a high risk of fetal and maternal morbidity, mortality, and FGR. Impaired VCT differentiation is a crucial feature of EOPE. The trophoblast defects cause incomplete spiral artery remodeling, leading to insufficient placental perfusion (*4*–*6*). To compensate for the insufficiency, the mother's blood pressure increases, a symptom of EOPE that usually manifests at the end of the second or third trimester. The symptoms subside when the placenta is expelled at delivery (*7*). The time gap between the onset of trophoblast cellular defects and the detection of disease phenotypes makes it challenging to study the etiology of EOPE (*8*). On the other hand, patients with late-onset PE have a normal placenta, and the condition is associated with maternal risk factors such as high body mass index and cardiovascular disorders (*9*).

At present, the use of the soluble FMS like tyrosine kinase 1 (sFlt-1): placental growth factor (PlGF) ratio for predicting PE in the second trimester has been suggested and used in clinical environments (*10*, *11*). Moreover, attempts have been made to use apheresis systems containing tetrameric vascular endothelial growth factor (VEGF) to absorb excess sFlt-1 in patients with PE (*12*). Despite

[1]Department of Obstetrics and Gynaecology, LKS Faculty of Medicine, The University of Hong Kong, Hong Kong, China. [2]Shenzhen Key Laboratory of Fertility Regulation, The University of Hong Kong-Shenzhen Hospital, Shenzhen, China. [3]BGI-Shenzhen, Shenzhen 518083, China. [4]College of Life Sciences, University of Chinese Academy of Sciences, Beijing 100049, China. [5]Shenzhen Engineering Laboratory for Birth Defects Screening, Shenzhen, China. [6]Stem Cell and Regenerative Medicine Consortium, School of Biomedical Sciences, LKS Faculty of Medicine, The University of Hong Kong, Hong Kong, China. [7]Department of Obstetrics and Gynaecology, Queen Mary Hospital, Hong Kong, China. [8]Department of Obstetrics and Gynaecology, Queen Elizabeth Hospital, Hong Kong, China. [9]Center for Energy Metabolism and Reproduction, Shenzhen Institute of Advanced Technology, Chinese Academy of Sciences, Shenzhen 518055, China. [10]Department of Obstetrics and Gynaecology, The Third Affiliated Hospital of Guangzhou Medical University, Guangzhou, China. [11]Department of Prenatal Diagnosis and Fetal Medicine, The Third Affiliated Hospital of Guangzhou Medical University, Guangzhou, China. [12]NHC Key Lab of Reproduction Regulation (Shanghai Institute of Planned Parenthood Research), Hospital of Obstetrics and Gynecology, Fudan University Shanghai Medical College, Shanghai, China.
*Corresponding author. Email: gaoya@genomics.cn (Y.G.); yaoyq@hku-szh.org (Y. Y.); pchiucn@hku.hk (P.C.N.C.)
†These authors contributed equally to this work.

these documented efforts, there is still no widely accepted clinically validated PE marker in the first trimester of pregnancy or prevention strategy or effective treatment for PE other than delivery. This is primarily due to our lack of complete understanding of the underlying pathophysiology (*13*, *14*).

Adrenomedullin (ADM) is a peptide hormone composed of 52 amino acids belonging to the calcitonin/calcitonin-gene-related peptide (CGRP)/amylin peptide family. ADM functions as a local paracrine and autocrine mediator of numerous physiological processes, including the regulation of cell growth and differentiation (*15*). In humans, plasma ADM levels are elevated after implantation, peaked in early pregnancy, and decreased at term (*16*–*18*). Its levels in the umbilical vein are higher than that in the umbilical artery, indicating a fetal origin of ADM. In animal studies, ADM-null mice (*19*) and the infusion of ADM^{22-52} (an ADM receptor antagonist) in pregnant rats (*20*) revealed that reduced ADM expression disrupts fertility, placentation, and fetal growth. Placental-specific ADM knockout (KO) and overexpression mouse models further showed that trophoblastic ADM is necessary for placental development by promoting the recruitment and activation of decidual natural killer (dNK) cells (*15*, *21*). However, the role of ADM in human placentation remains to be studied.

Our hypothesis is that trophoblastic ADM regulates human placental development by modulating trophoblast differentiation. The down-regulation of ADM contributes to the pathophysiology of EOPE. Our data provided evidence that defective trophoblastic ADM expression is a fetal cause of EOPE. Specifically, the defect affects the differentiation and activities of trophoblasts and thereby disrupts normal placental development. Clinically, the results of this study indicated the possible use of ADM in the early prediction of EOPE and that placenta-targeted delivery of ADM can potentially be applied for the treatment of EOPE.

RESULTS

Placental and circulating ADM levels are reduced in human and murine EOPE

EOPE is a condition that is specific to pregnancy and has a large impact on maternal and perinatal health worldwide, often leading to morbidity and mortality. Although early diagnosis, targeted surveillance, and timely delivery can help manage the condition, the lack of effective predictive tests for EOPE remains a challenge. Our team has specifically studied placenta-enriched molecule ADM as a potential biomarker to improve prediction. Here, we have generated a spatially resolved multi-omics single-cell atlas of human first-trimester villi (Fig. 1A and fig. S1, A to C), which enables us to resolve the full trajectory of ADM expression (Fig. 1A). We demonstrated a high ADM expression in the VCT and SCT during first trimester (Fig. 1A). Using immunostaining, we confirmed the consistent results of ADM expression in the outmost trophoblast layer of human first-trimester placental villi (Fig. 1B). Combined with the analysis of the single-cell RNA sequencing (scRNA-seq) dataset from human cell landscape (fig. S1D) (*22*) and early maternal-fetal interface (fig. S1E) (*23*), we confirmed the expression of ADM in VCT and SCT. Together, our data provided a comprehensive analysis of ADM expression of human trophoblast cell states in the first trimester.

To test the relevance of ADM expression to EOPE, we examined ADM expression in the serum of clinical samples, as well as in an L-NAME (Nω-nitro-L-arginine methyl ester hydrochloride)–induced PE mouse model. As the key pathogenic events in EOPE, including dysregulated trophoblast differentiation (*24*, *25*), take place in the first trimester of a pregnancy before the clinical onset of EOPE phenotypes, we determined the ADM expression in maternal serum samples and correlated the results with the occurrence of EOPE at delivery. In the study cohort, the EOPE women presented with proteinuria and significantly higher blood pressure when compared to the control with normotensive pregnancy (table S1). The birth weight and placental weight were significantly lower in the EOPE subjects. The maternal age, parity, and body mass index were comparable between the two groups. The MR-proADM (midregional proADM) is a surrogate marker of ADM. It is produced in a 1:1 ratio with mature ADM from ADM precursor and is more stable than ADM in blood and in extended storage. Enzyme-linked immunosorbent assay (ELISA) data showed that women with EOPE exhibited a lower serum level of MR-proADM, the early maternal serum from patients who subsequently developed EOPE in late pregnancy (Fig. 1C). In the L-NAME–induced PE mouse model, lower ADM expression was also found in the serum compared with control mice (Fig. 1D). Together, the reduction of ADM in the serum of patients with EOPE may have clinical utility in early detection of PE.

Chorionic villous sampling (CVS) entails sampling of the chorionic villous during 11 to 13 weeks of gestation for prenatal diagnosis. Immunostaining of the first-trimester chorionic villous revealed a significant down-regulation of ADM expression in the trophoblast layer of EOPE pregnancy when compared to that of normotensive pregnancy (Fig. 1E). A similar reduction of ADM immunoreactivities was found in placental tissues at delivery between normotensive and EOPE pregnancies (Fig. 1F).

The mature mouse placenta is composed of three layers: maternal decidua, junctional zone, and labyrinth. The labyrinth zone connects the placenta to the fetus. It consists of fetal and maternal blood spaces separated by vascular endothelium, trophoblast progenitor cells, and multinucleated SCTs. The junctional zone separates the labyrinth from the maternal decidua and consists of spongiotrophoblasts, glycogen trophoblasts, and a layer of trophoblast giant cells (TGCs) (*26*). While the spongiotrophoblasts and the glycogen trophoblasts are essential for the normal function of the placenta, their specific function remains unknown. The TGCs are equivalent to the human EVT and mediate invasion of the placenta into the maternal decidua. High ADM expression was found in the labyrinth zone and TGCs of the mouse placenta (Fig. 1G). Together, these data suggest that ADM expression is down-regulated in the placental villi and peripheral blood of PE subjects.

ADM regulates trophoblast differentiation into SCT and EVT in vitro

Because the etiology of EOPE is associated with defective VCT differentiation, we postulated that ADM was important for VCT differentiation. Physiological study of human trophoblast differentiation was almost impossible in the past because of the limited availability of primary human trophoblast in early pregnancy. This has recently become feasible with the establishment of trophoblast stem cells (TSCs) and trophoblast organoids.

Human expanded potential stem cells (hEPSCs) are a new type of stem cell with molecular and functional features of human embryos (*27*). hEPSC can be differentiated into embryonic lineages

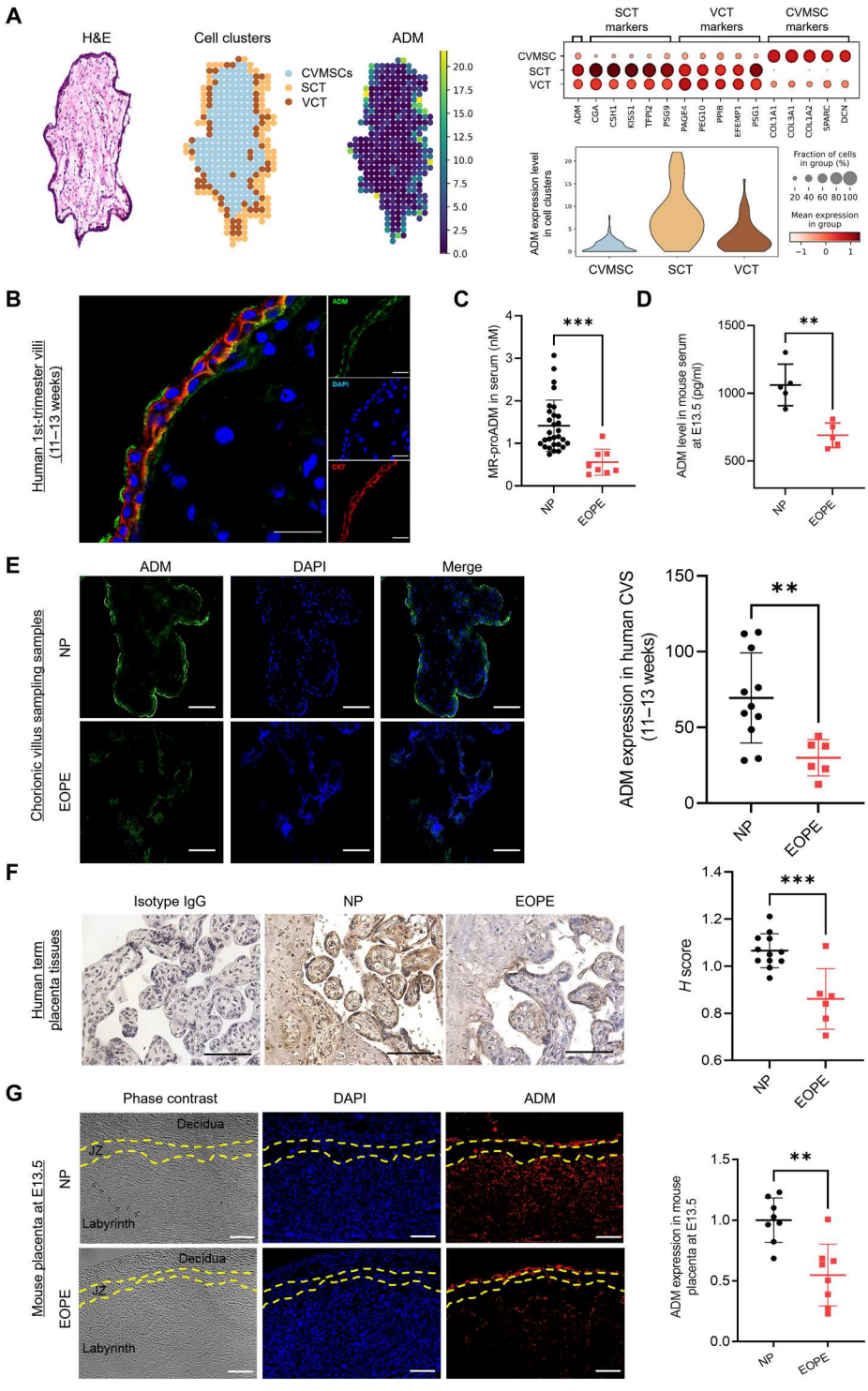

Fig. 1. Reduced placental and circulating ADM levels in human and murine EOPE. (**A**) Analysis of the spatial transcriptome of human first-trimester placenta villi. With the corresponding hematoxylin and eosin (H&E) staining, dot plots show the cluster assignments of main cell types and distribution of ADM in villi. The bubble chart shows the expression of known lineage-specific genes. Violin plots represent the expression levels of ADM in villi. CVMSC, chorionic villous mesenchymal stem/stromal cell. (**B**) Immunofluorescence staining of CK7 (red) and ADM (green) in human first-trimester placenta villi (left). Nuclei were counterstained with 4′,6-diamidino-2-phenylindole (DAPI; blue). Scale bars, 20 μm. (**C**) Quantification of MR-proADM in the early maternal serum from patients who subsequently developed EOPE in late pregnancy (n = 8) and from normotensive pregnant women (n = 80). (**D**) ADM concentration in serum of control and L-NAME–induced EOPE-like mice at embryonic day 13.5 (E13.5). (**E**) Immunofluorescence staining of ADM (green) in human normotensive and EOPE chorionic villous sampling (CVS) samples. Nuclei were counterstained with DAPI (blue). Scale bars, 200 μm. Quantification of ADM expression in CVS samples of EOPE (n = 4) and normotensive (n = 11) pregnancies. Each dot represents one subject's average ADM expression level of six random fields. (**F**) Immunohistochemistry staining and quantification of ADM in term placentas from patients with EOPE (n = 6) and from normotensive pregnant women (n = 12). Scale bars, 100 μm. (**G**) Immunofluorescence staining and quantification of ADM (red) in placentas of control and L-NAME–induced EOPE-like mice at E13.5. Nuclei were counterstained with DAPI (blue). N = 5 individual animals. NP, normotensive pregnancy; JZ, junctional zone. Scale bars, 200 μm. Data are represented as means ± SD. Statistical analysis was performed using unpaired Student's t test [(C) to (G)]. $^{**}P < 0.01$ and $^{***}P < 0.001$. IgG, immunoglobulin G.

and bona fide trophoblast (*27*). Critically, hEPSCs can be converted into VCT-like TSC lines capable of differentiation into EVT and SCT and permit efficient CRISPR-Cas9–based genome editing (*27*–*30*). To understand the role of ADM on trophoblast differentiation, TSC lines from hEPSCs were established. The derived TSC expressed specific trophoblast markers GATA binding protein 3 (GATA3) and integrin subunit alpha 5 (ITGA5) (fig. S2A) and were capable of differentiating into human leukocyte antigen G–positive (HLA-G$^+$) EVT (fig. S2, B and C) and human chorionic gonadotropin–positive (hCG$^+$) SCT in vitro (fig. S2D). Exogenous ADM treatment significantly enhanced differentiation of the TSC to EVT (fig. S3A) or SCT (fig. S3B). We then generated a TSC line with ($TSC^{ADM\ KO}$) or without ADM knockout (Fig. 2, A and B, and fig. S4, A to D) using CRISPR-Cas9. ADM knockout showed no effects

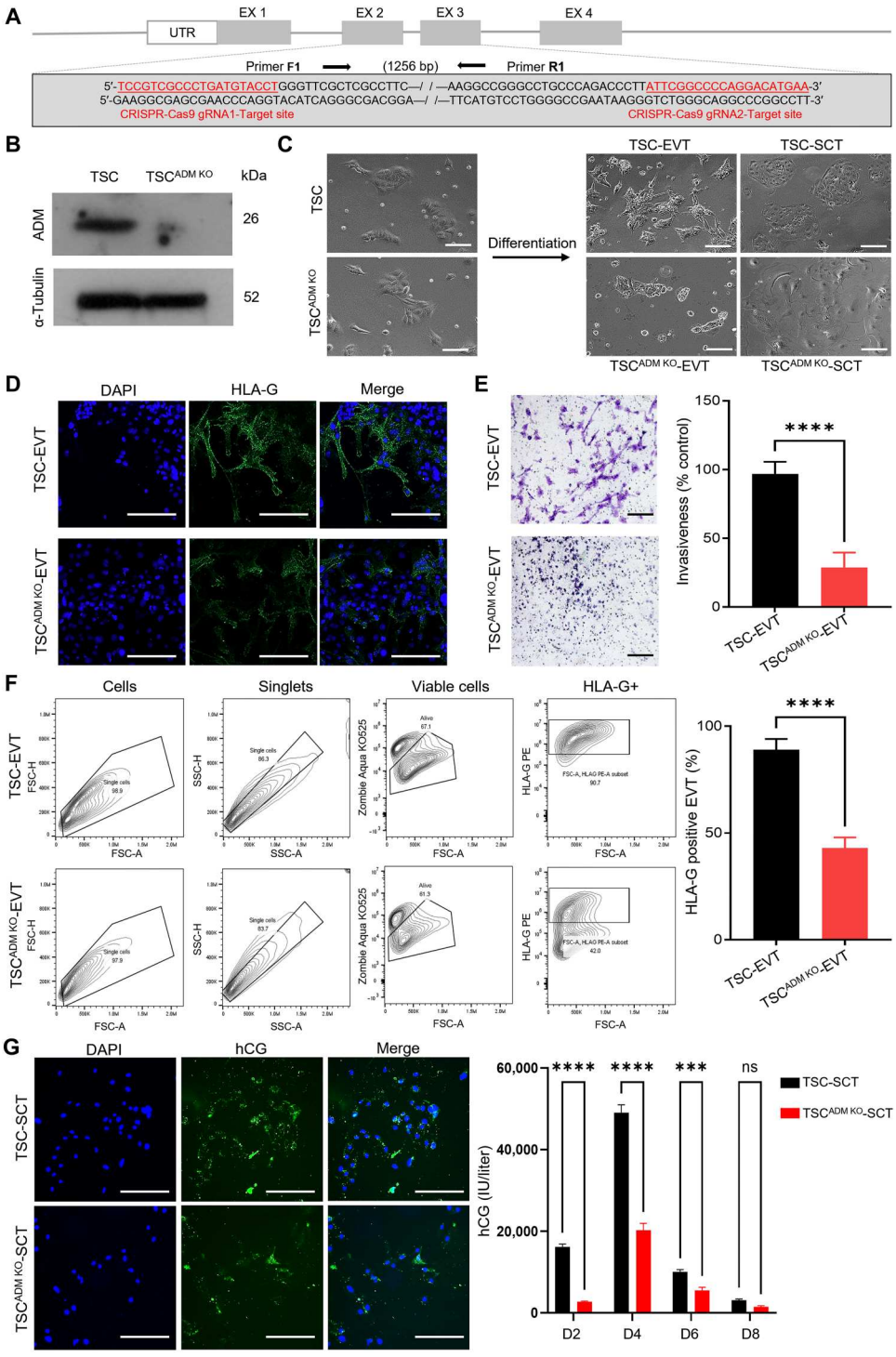

Fig. 2. Effect of ADM knockout in trophoblast differentiation into SCT and EVT. (**A**) ADM guide RNAs (gRNAs) for CRISPR-Cas9–mediated knockout of the human ADM gene. (**B**) Expressions of ADM were analyzed by Western blotting, with α-tubulin used as the internal control. $N = 5$. (**C**) Bright-field images of control TSC/TSC$^{ADM\ KO}$ differentiating toward EVT and SCT on day 6. Scale bars, 200 μm. (**D**) Immunofluorescence staining of EVTs differentiated from TSC/TSC$^{ADM\ KO}$ for EVT-specific marker HLA-G (green). Nuclei were counterstained with DAPI (blue). Scale bars, 200 μm. (**E**) Evaluation of the invasiveness of EVTs differentiated from control TSC/TSC$^{ADM\ KO}$ using the transwell invasion assay. The invaded cells on the lower surface were stained with crystal violet and were observed under a light microscope. Scale bars, 100 μm. $N = 5$. (**F**) Flow cytometric quantification of HLA-G expression in EVTs generated from control TSC/TSC$^{ADM\ KO}$. $N = 5$. (**G**) Immunofluorescence staining of SCTs differentiated from control TSC/TSC$^{ADM\ KO}$ for SCT-specific marker hCG (green). Nuclei were counterstained with DAPI (blue). Scale bars, 200 μm. Quantification of hCG in conditioned medium collected from SCT differentiated from TSC/TSC$^{ADM\ KO}$ on days 2, 4, 6, and 8 by immunoassay analyzer. $N = 5$. *N* indicates the number of independent experiments. Statistical analysis was performed using unpaired Student's *t* test [(E) and (F)], two-way analysis of variance (ANOVA) with Šídák's multiple comparisons tests (G). ***$P < 0.001$ and ****$P < 0.0001$. ns, not significant.

on TSC marker GATA3 (fig. S4E), cell viability (fig. S4F), and cell cycle progression (fig. S4G) of TSCs in vitro. ADM knockout significantly decreased EVT and SCT differentiation of TSC as shown by morphological analysis (Fig. 2C), reduced EVT lineage marker genes expression and invasion (Fig. 2, D to F), and reduced SCT lineage marker genes expression and hCG production (Fig. 2G). The reduced efficiency of differentiation of TSC$^{ADM\ KO}$ to EVT (Fig. 3A) or SCT (Fig. 3, B and C) was partially abrogated by the addition of exogenous ADM, suggesting autocrine functions of ADM in trophoblast differentiation. To address this possibility, TSCs were treated with ADM receptor antagonist ADM$^{22–52}$. The treatment significantly suppressed EVT (Fig. 3D) and SCT (Fig. 3E) differentiation of TSCs, as shown by the reduced expression of markers of EVT (*HLAG*) and SCT (*CGB*, *SDC1*, and *PSG1*). Similar observations were found in trophoblast organoids derived from early placental villi, where the administration of ADM

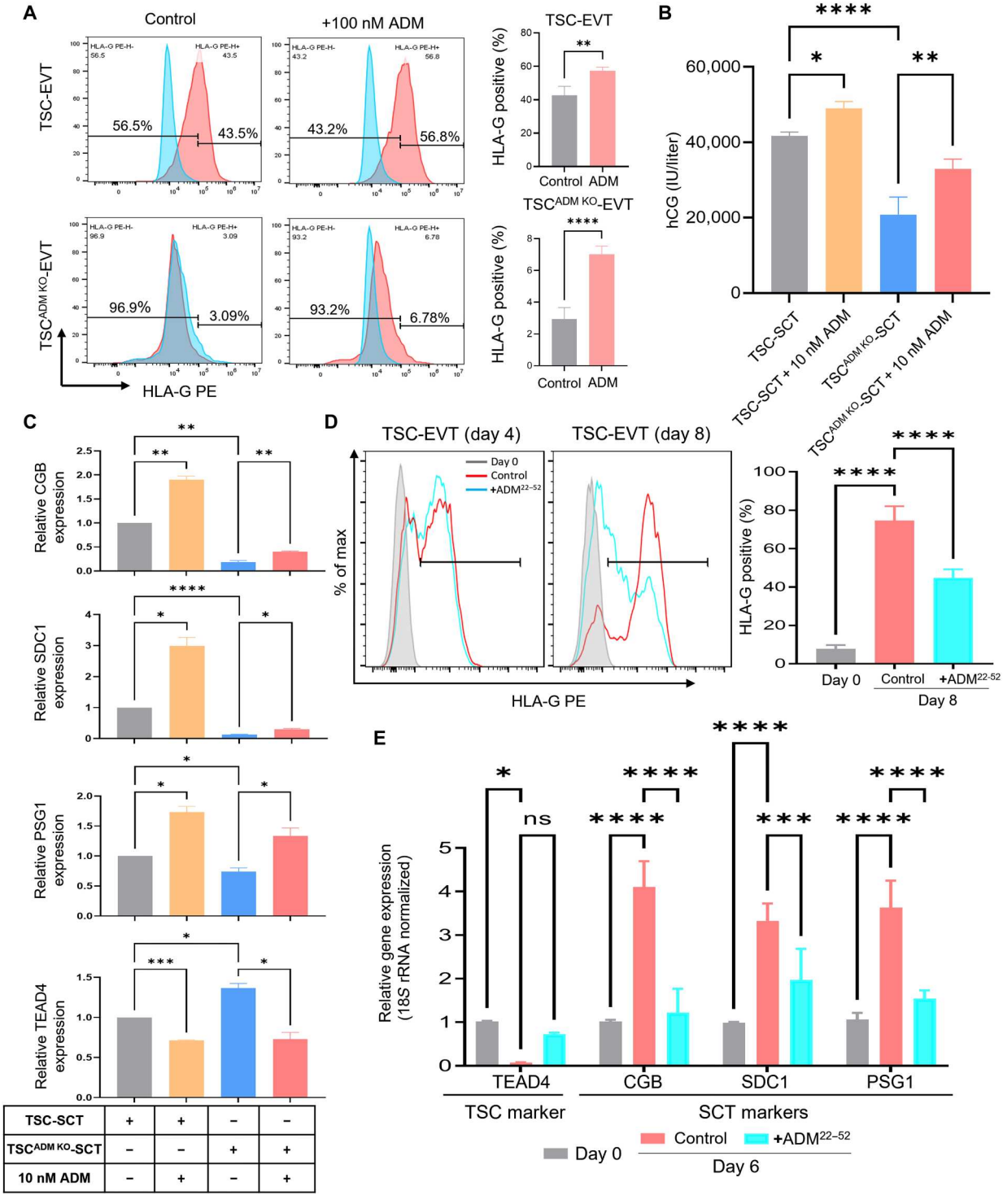

Fig. 3. The autocrine effect of ADM in the differentiation of TSC. (**A**) Flow cytometric quantification of HLA-G expression in EVTs generated from TSC/TSC$^{ADM\ KO}$ with ADM replenishment. $N = 5$. (**B**) Quantification of hCG by immunoassay analyzer in conditioned medium collected from SCT differentiated from TSC/TSC$^{ADM\ KO}$ with ADM replenishment. $N = 5$. (**C**) Quantitative polymerase chain reaction (qPCR) analysis of TSC marker [TEA domain transcription factor 4 (TEAD4)] and SCT markers (CGB, SDC1, and PSG1) in TSC differentiation toward SCTs with ADM replenishment. $N = 5$. (**D**) Flow cytometric quantification of HLA-G expression in EVTs generated from TSC with/without ADM$^{22–52}$ treatment on days 4 and 8. $N = 5$. (**E**) qPCR analysis of TSC marker (TEAD4) and SCT markers (CGB, SDC1, and PSG1) in TSC differentiation toward SCTs with/without ADM$^{22–52}$ treatment on day 6. $N = 5$. N indicates the number of independent experiments. Statistical analysis was performed using unpaired Student's t test (A), one-way ANOVA with Holm-Šídák's multiple comparison tests [(B) to (D)], and two-way ANOVA with Tukey's multiple comparisons tests (E). $^*P < 0.05$, $^{**}P < 0.01$, $^{***}P < 0.001$, and $^{****}P < 0.0001$. rRNA, ribosomal RNA.

significantly promoted, while that of ADM$^{22–52}$ blocked, trophoblast differentiation (EVT: Fig. 4A; SCT: Fig. 4B).

To better understand the effects of ADM on trophoblast fate specification, we performed transcriptome profiling of TSC and TSC$^{ADM\ KO}$ before and after EVT/SCT differentiation using RNA-seq. The resemblance between in vitro generated trophoblasts (TSC, TSC-EVT, and TSC-SCT) and the in vivo trophoblasts was supported by mapping our in vitro bulk RNA-seq to the in vivo scRNA reference (*23*) with singular value decomposition modeling (Fig. 5A). We next investigated global gene transcriptional changes in TSC$^{ADM\ KO}$. Hierarchical cluster and principal components analysis revealed that the TSC$^{ADM\ KO}$, TSC$^{ADM\ KO}$-EVT, or TSC$^{ADM\ KO}$-SCT were clustered together and separated from the corresponding controls (Fig. 5, B and C). Differentially expressed genes were identified between the TSC and TSC$^{ADM\ KO}$ and their differentiated progenies on days 2 and 4 (Fig. 5D). Among the differentially expressed genes, there were many transcription factors known to be associated with trophoblast differentiation (Fig. 5E), indicating a possible developmental disturbance of TSC after the ADM knockout. The differentially expressed genes were subjected to gene ontology enrichment analyses. The top 15 enriched categories are shown in (Fig. 5F). As expected, many of the enriched biological processes were related to cell development. Kyoto Encyclopedia of Genes and Genomes (KEGG) pathway analysis revealed an enrichment of genes associated with extracellular matrix–receptor interaction, focal adhesion, and phosphatidylinositol 3-kinase (PI3K)–AKT signaling pathway (Fig. 5F), which were crucial in trophoblast differentiation. Some differentially expressed transcription factors, such as signal transducer and activator of transcription 1 (STAT1) and forkhead box O1 (FOXO1), were downstream of the PI3K/AKT signaling pathway (Fig. 5E). Overall, these data reveal that the trophoblastic ADM regulates human trophoblast differentiation to EVT and SCT.

Trophoblastic ADM knockdown induces defective placental development and EOPE-like phenotypes in pregnant mice

To define the role of ADM on placental development in vivo, we used the placenta-targeted nanoparticle model to knockdown ADM expression, specifically in mouse trophoblasts. Synthetic chondroitin sulfate A (CSA) binding peptide (plCSA-BP) specifically binds to a distinct placental-type CSA on trophoblasts. The conjugation of plCSA-BP to lipid-polymer nanoparticles could effectively deliver the payloads to the trophoblast target (*31*, *32*). In this study, we loaded the nanoparticles with ADM morpholino (ADM Mor-NPs) or ADM morpholino with five mismatch pairs (Control Mor-NPs; fig. S5A) (*27*). The shape and size distributions of the ADM Mor-NPs and the Control Mor-NPs were similar as determined by dynamic light scattering analysis and electronic microscopy (fig. S5, B and C). ADM/Control Mor-NPs (50 μg/kg) were intravenously injected into pregnant mice on embryonic day 5.5 (E5.5), E7.5, and E9.5 (fig. S5D). They were taken up by the trophoblasts in the labyrinth zone after 48 hours as indicated by the

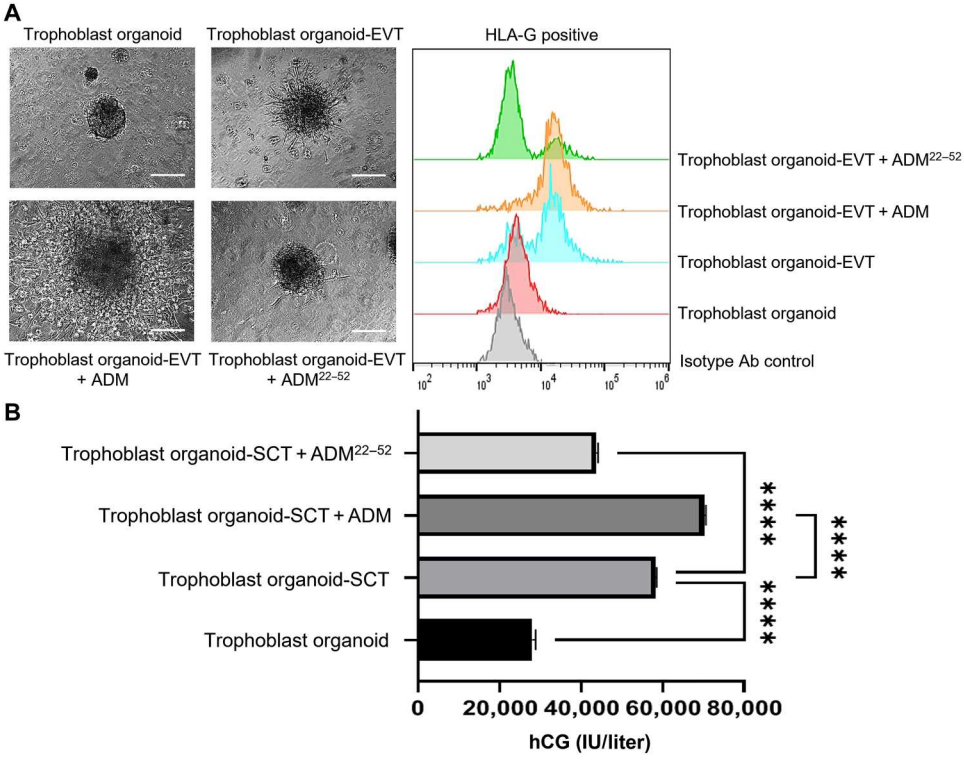

Fig. 4. Assessment of ADM in the differentiation of human trophoblast organoids. (**A**) Bright-field images of EVT differentiation of human trophoblast organoids with/without ADM and ADM$^{22–52}$. Scale bars, 200 μm. Flow cytometric quantification of HLA-G expressions in EVTs generated from trophoblast organoids with/without ADM and ADM$^{22–52}$. $N = 5$. (**B**) Quantification of hCG by immunoassay analyzer in conditioned medium collected from SCT differentiation of human trophoblast organoids with/without ADM and ADM$^{22–52}$ treatment. $N = 5$. *N* indicates the number of independent experiments. Statistical analysis was performed using one way ANOVA with Šídák's multiple comparisons tests. ****$P < 0.0001$. Ab, antibody.

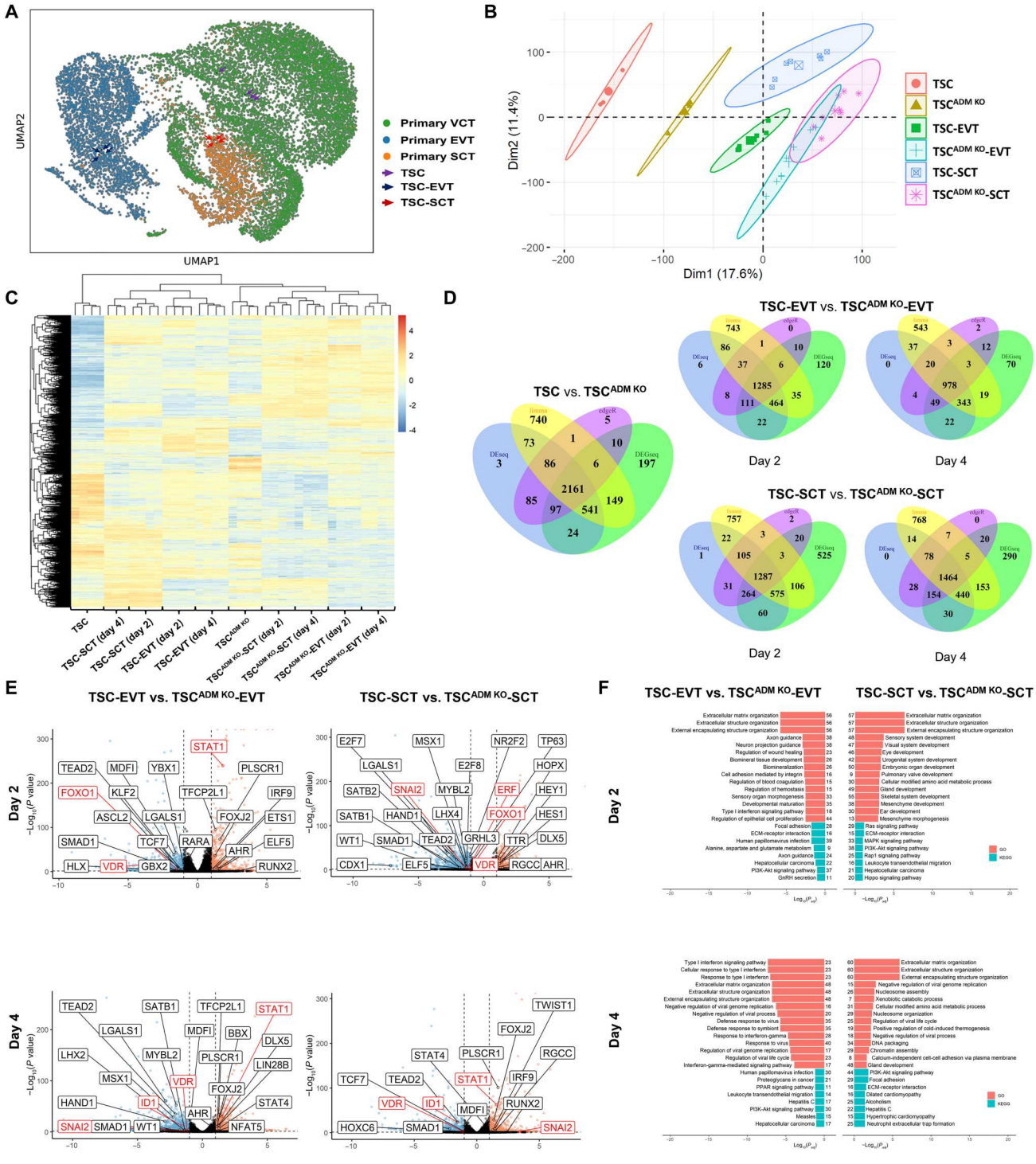

Fig. 5. Differentially expressed genes and differentiated progenies between TSC and TSC$^{ADM\ KO}$. (**A**) TSC-derived trophoblast cell clusters are close to primary trophoblasts. Comparison of RNA transcriptomes between placental primary trophoblasts (VCT, EVT, and SCT) and TSC-derived trophoblasts (TSC, EVT-TSC, and SCT-TSC). (**B**) Transcriptomic profiling of control TSC and TSC$^{ADM\ KO}$ before and after EVT/SCT differentiation using RNA-seq. Principal components analysis for control TSC/TSC$^{ADM\ KO}$ (TSC, SCT, and EVT). $N = 5$. (**C**) Heatmap shows hierarchical clusters based on the magnitude of trophoblastic gene signatures in control TSC/TSC$^{ADM\ KO}$ at days 0, 2, and 4. Genes are ordered by expression in respective gene sets, and samples are ordered by cluster result. Expression is normalized by dividing the mean of expression and $\log_2$-transformed. (**D**) The Venn diagram shows the overlap genes of the core portion of the TSC/TSC$^{ADM\ KO}$ and EVT and SCT derived from control TSC/TSC$^{ADM\ KO}$ at days 0, 2, and 4. (**E**) Volcano plots of gene expression in transcriptome profiling of EVT and SCT derived from control TSC/TSC$^{ADM\ KO}$ on days 2 and 4. Significantly up-regulated and down-regulated genes are highlighted in orange and blue, respectively. Transcriptional factors are labeled in black boxes, and genes related to PI3K are labeled in red boxes. Data are shown as means ± SD. $N = 5$. (**F**) Gene Ontology (GO) and KEGG analysis for shared up-regulated and down-regulated genes in EVT and SCT derived from TSC/TSC$^{ADM\ KO}$ at days 0, 2, and 4. $N = 4$ independent experiments. *N* indicates the number of independent experiments.

colocalization of the trophoblast marker cytokeratin 7 (CK7) and ADM Mor-NPs (fig. S5, E to G). The tested dose seems to be well tolerated by the animals, as indicated by normal histological examinations of the heart, liver, spleen, lung, and kidney following nanoparticle administration (fig. S5H). This observation aligns with the findings of a previous study (*33*).

ADM Mor-NP significantly suppressed the expression of trophoblastic ADM protein in the mouse placenta when compared with the Control Mor-NP (Fig. 6A and fig. S6A). The ADM Mor-NP group exhibited extensive placental hemorrhage, partial fetal demise, resorption on E11.5 and E13.5 (Fig. 6B), and complete fetal resorption on E15.5 to E17.5 (fig. S6B). Increase in maternal blood pressure (Fig. 6C), decrease in maternal body mass, fetal

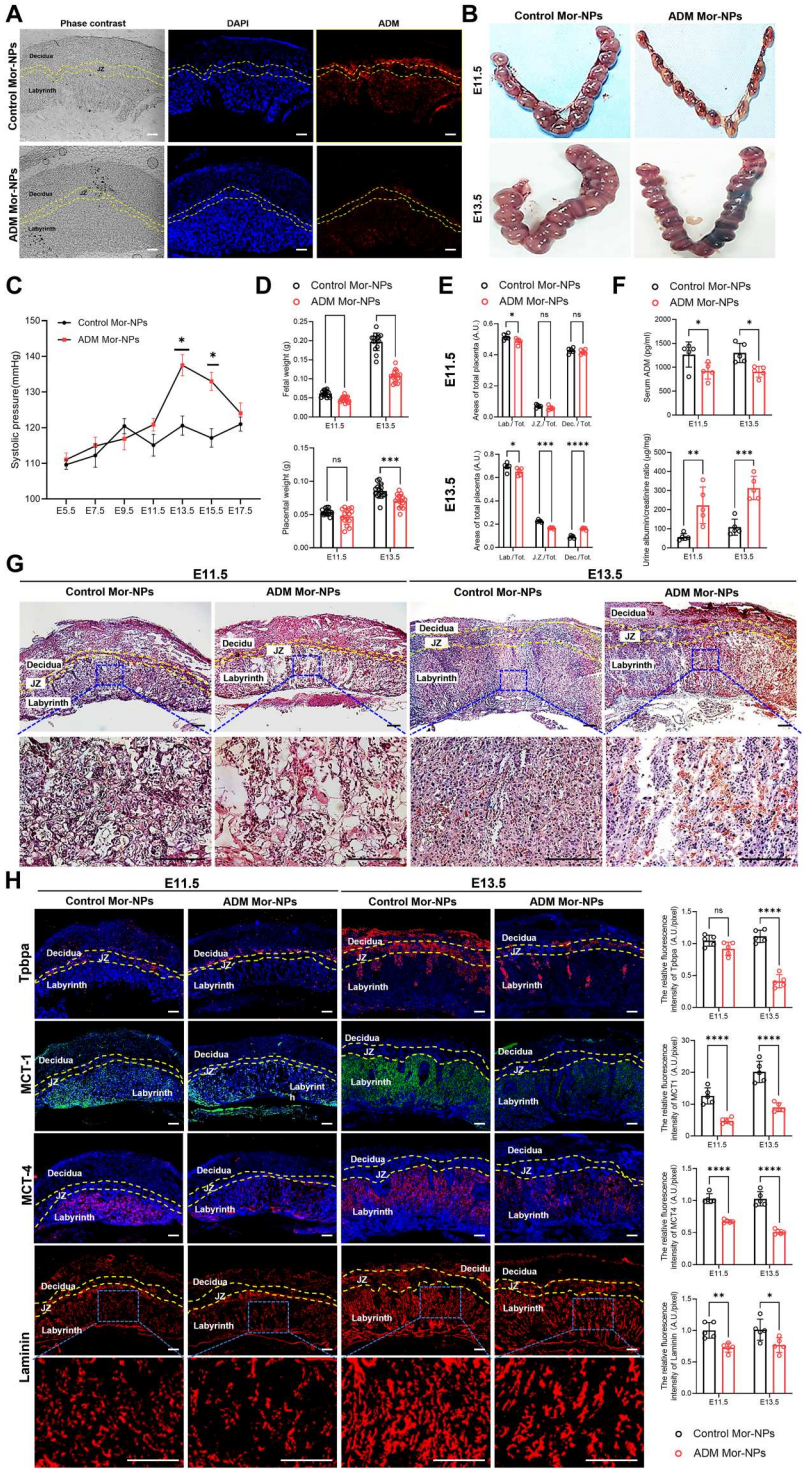

Fig. 6. Defective placental development and EOPE-like phenotypes in trophoblast-specific ADM knockdown mice. (**A**) Immunofluorescence images of ADM expression (red) in mouse placentas at E11.5. Nuclei were counterstained with DAPI (blue). Scale bars, 200 μm. (**B**) Images of the mouse uteri at E11.5 and E13.5. (**C**) Systolic blood pressure in the pregnant mice. $N = 4$. (**D**) Fetal and placental weights at E11.5 and E13.5. Placentas were weighed subsequent to the removal of the umbilical cord and fetal membranes. $N = 5$. (**E**) Ratios of placental zones (labyrinth, JZ, and decidua) to total placental areas at E11.5 and E13.5. (**F**) Serum ADM level and the urinary albumin and creatinine ratio at E11.5 and E13.5. (**G**) H&E staining of the cross section of the placentas at E11.5 and E13.5. Perimeters of placental zones (labyrinth, JZ, and decidua). Scale bars, 200 μm (top) and 100 μm (bottom). (**H**) Immunofluorescence staining of TPBPA (spongiotrophoblasts and glycogen cells), MCT1 (SCT layer I), MCT4 (SCT layer II), and basement membrane component laminin (demarcates fetal blood vessels) expression in mice. The quantification of immunofluorescence intensity was analyzed with ImageJ, and signal intensity was normalized to the pixel area of the image. Nuclear counterstain with DAPI. Scale bars, 200 μm. $N = 5$. *N* indicates the number of individual animals. Data are shown as means ± SD. Statistical analysis was performed using two-way ANOVA with the Geisser-Greenhouse correction test (C) and two-way ANOVA with Šídák's multiple comparisons tests [(D) to (F) and (H)]. $^{*}P < 0.05$, $^{**}P < 0.01$, $^{***}P < 0.001$, and $^{****}P < 0.0001$. A.U., arbitrary units.

and placental weight (fig. S6C and Fig. 6D), placental area (Fig. 6E), serum ADM level, and albumin/creatinine ratio in urine (Fig. 6F) were observed in the trophoblastic ADM knockdown mice on E11.5 and E13.5. Histopathological analysis revealed decreased labyrinth and junctional zone areas (Fig. 6G) and placental necrosis with accompanying expansion of intervillous space (Fig. 6G). Consistently, the densities of trophoblast-specific protein α–positive ($TPBPA^+$) invasive TGCs in the junctional zone (*26*), monocarboxylate transporter 1–positive ($MCT1^+$) SCTs layers I (Syn TI) cells, $MCT4^+$ SCTs layers II (Syn TII) cells in the labyrinth zone, and laminin-positive fetal-derived blood vessels were decreased in the trophoblastic ADM knockdown mice (Fig. 6H), suggesting defective placental development. Collectively, these data indicate that the trophoblastic ADM knockdown in mice causes defective placentation, resulting in typical EOPE symptoms.

Placenta-specific delivery of ADM ameliorates EOPE symptoms in L-NAME–induced PE mouse model

We next investigated whether ADM administration could be a potential treatment for EOPE phenotypes. We overexpressed ADM specifically in the placenta of the L-NAME–induced PE mouse model by injecting the plCSA-BP–coated nanoparticles loaded with ADM-modified mRNA (ADM-MNP; fig. S7A) on E6.5, E8.5, E10.5, and E12.5. ADM-MNP significantly enhanced the trophoblastic ADM level when compared with the control group on E13.5 (Fig. 7A and fig. S7B). Our results showed that forced trophoblastic ADM expression increased maternal body weight (fig. S7C), fetus size (Fig. 7B) and weight (Fig. 7C), and placenta weight (Fig. 7C) and decreased blood pressure (Fig. 7D) in the L-NAME–induced PE mice. The serum ADM level (Fig. 7E) and urine albumin/creatinine ratio (Fig. 7E) of the ADM-MNP–treated PE mice were also significantly lower than those of the control mice. Pathological changes in placenta structures, for example, increased the amount of syncytial knots, in the PE mice were effectively prevented by trophoblastic ADM induction (Fig. 7F and fig. S7D). Moreover, the EOPE symptoms associated with dysregulated trophoblast differentiation, including $TPBPA^+$ invasive trophoblast giant cell (Fig. 7G) and $MCT1/4^+$ Syn TI/II reduction (Fig. 7G), and trophoblastic PI3K-AKT signaling pathway disorders (Fig. 7H and fig. S7, E and F) were rescued by the ADM-MNP administration. All these data demonstrate that targeting trophoblastic ADM might be an attractive therapeutic strategy for EOPE.

DISCUSSION

The etiology of EOPE is associated with defective trophoblast differentiation and functions. The present study provides novel insights into the pathogenesis and targets for intervention of EOPE. By using the latest in vitro organoid culture and in vivo nanotechnology and by correlating these findings with that in the clinical EOPE samples, we demonstrated that trophoblastic ADM regulates placental development in humans by modulating trophoblast differentiation, and down-regulation of ADM contributes to the pathophysiology of EOPE. Our data also suggested the use of serum MR-proADM as an EOPE predictor and placental ADM as a target for placenta-specific nanoparticle-based treatment of EOPE.

During early pregnancy, ADM is predominantly expressed in the placenta. It is also expressed in all vascular tissues at the maternal-fetal interface (*21*). Here, we localized ADM expression to the VCT and SCT of placental villi from early human pregnancy, in line with reports on expression of ADM in trophoblast cell lines and primary trophoblasts (*34*). Our study also reported the quantification of ADM expression in trophoblast subtypes during early pregnancy by spatial and single-cell transcriptome. Immunostaining of CVS at 11 to 13 weeks of gestation and term placenta from EOPE pregnancies demonstrated a remarkable decrease in ADM expression at the maternal-fetal interface. The down-regulated ADM expression in CVS samples could be valuable for diagnosing EOPE in early pregnancy. CVS, a procedure used for fetal karyotype analysis, has excellent potential for predicting pregnancy complications and investigating human placentation (*35*, *36*). Compared with normotensive pregnancies, CVS samples of EOPE pregnancies exhibit differential gene expressions, such as VEGF (*VEGFA*), VEGFA receptor 1 (*Flt-1*), and superoxide dismutase (*SOD*) (*37*). Our discovery of reduced ADM expression in CVS demonstrated its predictive value for diagnosing EOPE in early pregnancy.

The decrease of ADM levels in EOPE clinical samples may result from a combination of factors. Embryo implantation into the uterine endometrium is essential for human development, and this process begins with blastocyst attachment to the endometrial epithelium (*38*). Both in vitro and in silico models of the epithelial phase of human embryo implantation reveal that interactions with endometrial epithelial cell promote trophoblast differentiation (*39*). Dysregulated implantation process is associated with the development of PE (*40*). Recent research also suggests that implantation and early pregnancy is a proinflammatory state (*41*). There is a high level of proinflammatory cytokines, such as tumor necrosis factor–α, interleukin-1β (IL-1β), and IL-6, in the environment. This network of cytokines is thought to play a role from conception to implantation and allows for the adaptation of the embryo to its new microenvironment (*41*). ADM production is strongly stimulated by these proinflammatory cytokines (*42*). Therefore, it is possible that dysregulated implantation process and uterine immune environment can lead to reduced ADM production and, thereby, aberrant placental development as demonstrated in our study.

The placenta releases peptides, small proteins, nucleic acids, mRNA, and noncoding RNA into maternal circulation. In the literature, ADM levels in maternal plasma of patients with EOPE are inconsistent, probably because of rapid clearance of ADM in body fluid, leading to significant variations of results among studies (*15*). MR-proADM is produced in a 1:1 ratio with mature ADM and is highly stable in serum (*43*, *44*). In addition, the validity of using MR-proADM as a useful clinical marker has been proven in sepsis (*45*), heart failure (*46*), and acute pulmonary embolism (*47*). Unlike ADM, which has autocrine and paracrine actions, MR-proADM has no reported physiological effect. Moreover, our results revealed reduced serum MR-proADM levels in patients with EOPE during early pregnancy. Therefore, serum MR-proADM can be a surrogate marker of ADM in predicting EOPE during early pregnancy.

Early detection of PE is essential, as it enables aspirin prophylaxis, intensive maternal, and fetal monitoring and ultimately prevents adverse outcomes for both the mother and the fetus (*48*). Angiogenic factors such as PlGF, ratio of sFlt-1 to PlGF, or their combination with clinical parameters have been used for early second-trimester PE screening (*49*). However, the performance of these algorithms or parameters varies significantly among populations and laboratories

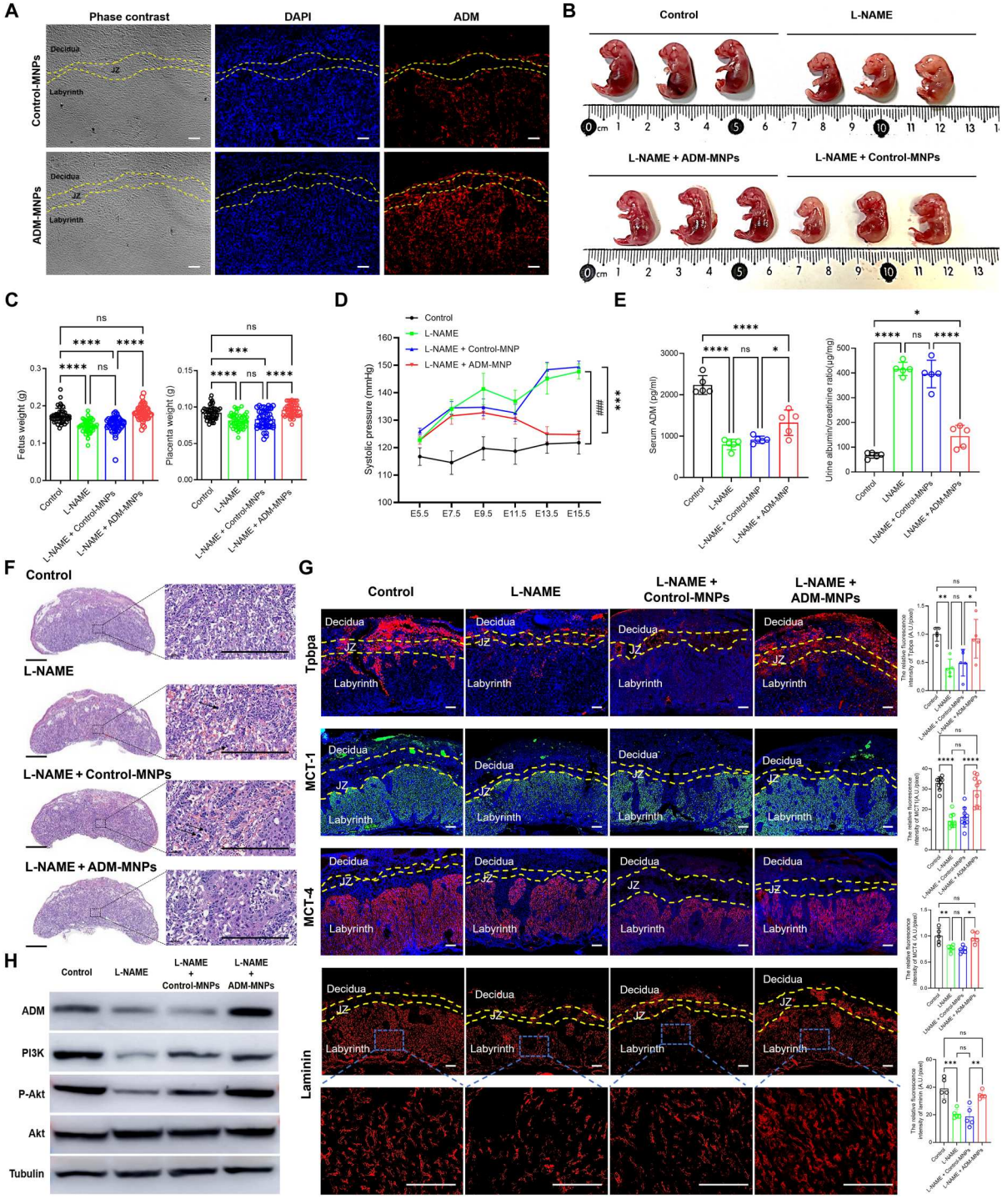

Fig. 7. Therapeutic delivery of trophoblast-specific ADM in the L-NAME–induced PE-like mouse model. (**A**) Immunofluorescence images of ADM expression (red) in mouse placentas at E13.5 in control, L-NAME, L-NAME + Control-MNP, and L-NAME + ADM-MNP groups. Scale bars, 200 μm. (**B**) Images of mouse fetuses at E15.5 in different groups. (**C**) Fetal and placental weights for each embryo at E13.5 in different groups. $N = 5$. (**D**) Systolic blood pressure in the pregnant mice in different groups. $N = 4$. (**E**) Serum ADM level and the urinary microalbumin and creatinine ratio at E13.5 in different groups. $N = 5$. (**F**) H&E staining images of the cross section of the placentas at E13.5 in different groups. The black arrows indicate the syncytial knots. Scale bar, 800 μm (left) and 50 μm (right). $N = 5$. (**G**) Immunofluorescence staining of TPBPA, MCT1, MCT4, and basement membrane component laminin expression in different groups. The images were analyzed with ImageJ, and signal intensity was normalized to the pixel area of the image. $N = 5$. (**H**) Expressions of phosphorylated PI3K, Akt, phosphorylated Akt, and ADM in different groups were analyzed by Western blotting. α-Tubulin was used as the internal control. $N = 5$. Nuclei were counterstained with DAPI (blue). *N* indicates the number of individual animals. Data are shown as means ± SD. Statistical analysis was performed using one-way ANOVA with Holm-Šídák's multiple comparisons test [(C) and (E)], two-way ANOVA with the Geisser-Greenhouse correction test (D), and one-way ANOVA with Šídák's multiple comparisons test (G). $^{*}P < 0.05$, $^{**}P < 0.01$, $^{***}P < 0.001$, and $^{****}P < 0.0001$; ###$P < 0.001$, L-NAME+ADM-MNP versus L-NAME + Control-MNP.

(*50*). There is a need of identifying new biomarkers for definitive early prediction of PE. New first-trimester biomarkers combined with clinical risk factors such as mean arterial blood pressure, uterine artery Doppler measurements, and urine protein have been validated for early prediction of PE (*51*). We showed that serum MR-proADM levels during the first trimester could potentially be incorporated into the current algorithms to predict PE. Compared to the most studied predictor, sFlt-1, which can be detected at 29 to 32 weeks of gestation (*52*), a decreasing level of circulating MR-proADM level at 11 to 16 weeks in pregnant women could allow early detection of PE, and therefore, earlier intervention can be offered to the patients. This potential use of ADM for early detection of PE needs to be validated with larger studies to explore its diagnostic performance on top of or in replacement with other markers.

Although the mouse placenta differs from the human placenta in morphogenesis and endocrine functions (*53*), mouse models are still primarily used to study human placental development and pregnancy complications such as PE because of their genetic homogeneity, similarity in molecular mechanisms of placental development, and ease of genomic manipulation (*54*). A wide range of PE models, including the spontaneous PE model, nitric oxide synthase inhibition model, angiogenesis factor imbalance model, oxygen stress model, immune response model, and vascular injury model have been developed to study the complex pathogenesis and symptoms of PE. In this study, L-NAME was used to induce EOPE-like phenotypes, which are highly similar to the clinical manifestations, pathological changes, oxidative stress, and inflammatory responses of EOPE (*55*). We acknowledge that it is unlikely that one model alone would be able to cover all aspects of EOPE pathogenesis. However, the L-NAME model is relatively simple and more accessible and allows time-dependent monitoring of changes in placenta, vasculature, and kidney during pregnancy (*55*). This model has also been used to study the therapeutic potential of various compounds. Here, we demonstrated the association of decreased placental ADM expression with manifestations of EOPE-like phenotypes in this model. The phenotypes were relieved by increasing ADM specifically in the trophoblast of the mice.

ADM global knockout causes intrauterine fetal lethality in mice (*56*), which is highly due to placental defects (*57*). To gain insights into trophoblast-derived ADM effects on placental development, trophoblast-specific knockdown of ADM in vivo was performed. Currently, manipulating placental gene expression in vivo requires transgenic animal technology, which is labor-intensive and time-consuming (*58*). Thus, we optimized a nanoparticle-based system for manipulating gene expression, specifically in the placenta in vivo (*33*). Nanoparticle-mediated trophoblastic ADM knockdown resulted in premature lethality of embryo at E15.5 and reduced fetal blood vessel branching in the labyrinth, recapitulating phenotypes observed in the ovary transplantation model, which showed that the loss of fetal ADM contributes to premature death of embryos and dysregulated fetal blood morphology (*21*). Both nanoparticle-induced ADM knockdown and fetal-specific knockout of ADM result in premature death in a similar time frame (*21*). Histological examination of the E11.5 and E13.5 placentas showed impaired Syn T layers formation (including SynT-I and SynT-II), reduced labyrinth layer, malformation of fetal blood vessels, and markedly reduced weights of the placentas and fetuses. These abnormalities collectively caused FGR and perinatal lethality. Disruption of either SynT-I or SynT-II layer by targeting syncytin-A– and syncytin-B–induced premature death and growth retardation (*59*, *60*) with phenotypes similar to that observed in the ADM mutant mice (*21*) and our trophoblastic-specific ADM knockdown mice. The relationships between ADM and the two syncytins in controlling trophoblast fusion and placental development are unclear and remain to be investigated.

Recent studies suggest that ADM has specific roles in the differentiation of several stem/progenitor cells (*61*), including the neural, hematopoietic, and rat TSCs. In our study, ADM-null TSCs failed to express markers of SCT and EVT upon differentiation, although their self-renewal ability was not affected. The differentiation defects might contribute to the labyrinth formation phenotype in the L-NAME–induced PE mouse model. ADM is best known to activate the PI3K-AKT pathway, which has been implicated in trophoblast differentiation (*62*). AKT inactivation results in disrupted trophoblast cell differentiation toward EVT (*63*). ADM-null TSC displayed reduced expression of genes related to PI3K-AKT signaling upon differentiation. Further mechanistic study regarding the ADM-PI3K-Akt pathway may shed light on the mechanism of TSC differentiation.

Using both loss-of-function and gain-of-function genetic mouse models, previous studies had found that trophoblastic ADM promoted appropriate recruitment and activation of maternal dNK cells to the placenta and thereby facilitate the remodeling of maternal uterine spiral arteries (*21*). However, there are only limited studies available exploring the direct association between dNK cells and trophoblast differentiation. Some studies indicated the active participation of dNK cells in the process of EVT differentiation toward endothelial phenotype (*64*). Therefore, whether dNK cells contribute to the regulatory role of ADM on trophoblast differentiation needs further investigation.

There is currently no effective treatment for PE or other placenta-associated diseases. Modified mRNA-based protein expression is a novel strategy for prevention and treatment of protein-based diseases by providing precise and personalized medicine, while there is a lack of effective and specific delivery approaches (*65*, *66*). Previous research has investigated nanoparticles as effective transport and delivery systems with minimal off-target effect, reduced toxicity, and improved biodistribution when compared to convenient administration routes (*67*). Nanoparticles in the form of liposomes, polymeric nanoparticles, or dendrimers have also been tested for the treatment of pregnancy complications (*68*). In this study, we demonstrated that targeted delivery of ADM mRNA to trophoblasts using nanoparticles successfully ameliorated proteinuria, relieved FGR and placental dysplasia, rescued differentiation of trophoblasts, and improved disordered fetal vessels in the L-NAME–induced PE mouse model. In the long run, nanoparticle technologies could be used to develop novel treatments for various pregnancy-associated complications (*68*).

One major limitation in using placenta-targeted delivery of ADM mRNA as a therapy approach for EOPE is that the treatment in the current study was started at E6.5 in mice, which is equivalent to weeks 5/6 in human gestation. However, despite decades of intense research on PE, there is still no pregnancy screening test available at such an early stage of pregnancy to recognize those at risk of EOPE. Therefore, although our results provide proof-of-concept validation on the treatment of EOPE using nanotechnology-based placental-specific gene manipulation, the methodology

still needs improvements such as increasing the cellular uptake efficiency of nanoparticles using triangular and rod-shaped nanoparticles (*69*).

Together, the present study demonstrates that ADM regulates human placental development by modulating trophoblast differentiation and placental insufficiency in ADM contributing to the pathophysiology of EOPE (Fig. 8). The importance of our findings may therefore extend to not only being a potential early predictive biomarker but also the establishment of a nanoparticle delivery system as a novel treatment strategy for EOPE (Fig. 8). This powerful tool is potentially useful for understanding the pathogenesis and as a treatment of developmental disorders with trophoblast defects other than EOPE such as miscarriage and intrauterine growth restriction.

MATERIALS AND METHODS

Study subjects and the collection of CVS tissue samples, maternal serum, and term placental tissue

The involvement of human subjects in this study was approved by the Institutional Review Board (IRB UW20-060) of The University of Hong Kong/Hospital Authority Hong Kong West Cluster. Women with EOPE and normotensive pregnancy (NP) were recruited in the third trimester from March 2017 to March 2022 in the Department of Obstetrics and Gynaecology, Queen Mary Hospital.

EOPE was defined as hypertension (systolic blood pressure or diastolic blood pressure of ≥140 or ≥90 mm Hg on two occasions at least 4 hours apart) and significant proteinuria (≥300 mg of protein per 24 hours of urine collection or protein/creatinine ratio of ≥0.3 mg/dl or dipstick reading of 2+ in a random urine sample) after 20 weeks and before 34 weeks of gestation in a woman with a previously normal BP. Exclusion criteria were (i) diabetes mellitus, (ii) chronic hypertension, (iii) renal diseases, (iv) autoimmune diseases, (v) cardiovascular diseases, and (vi) chronic hypertension complicating pregnancy.

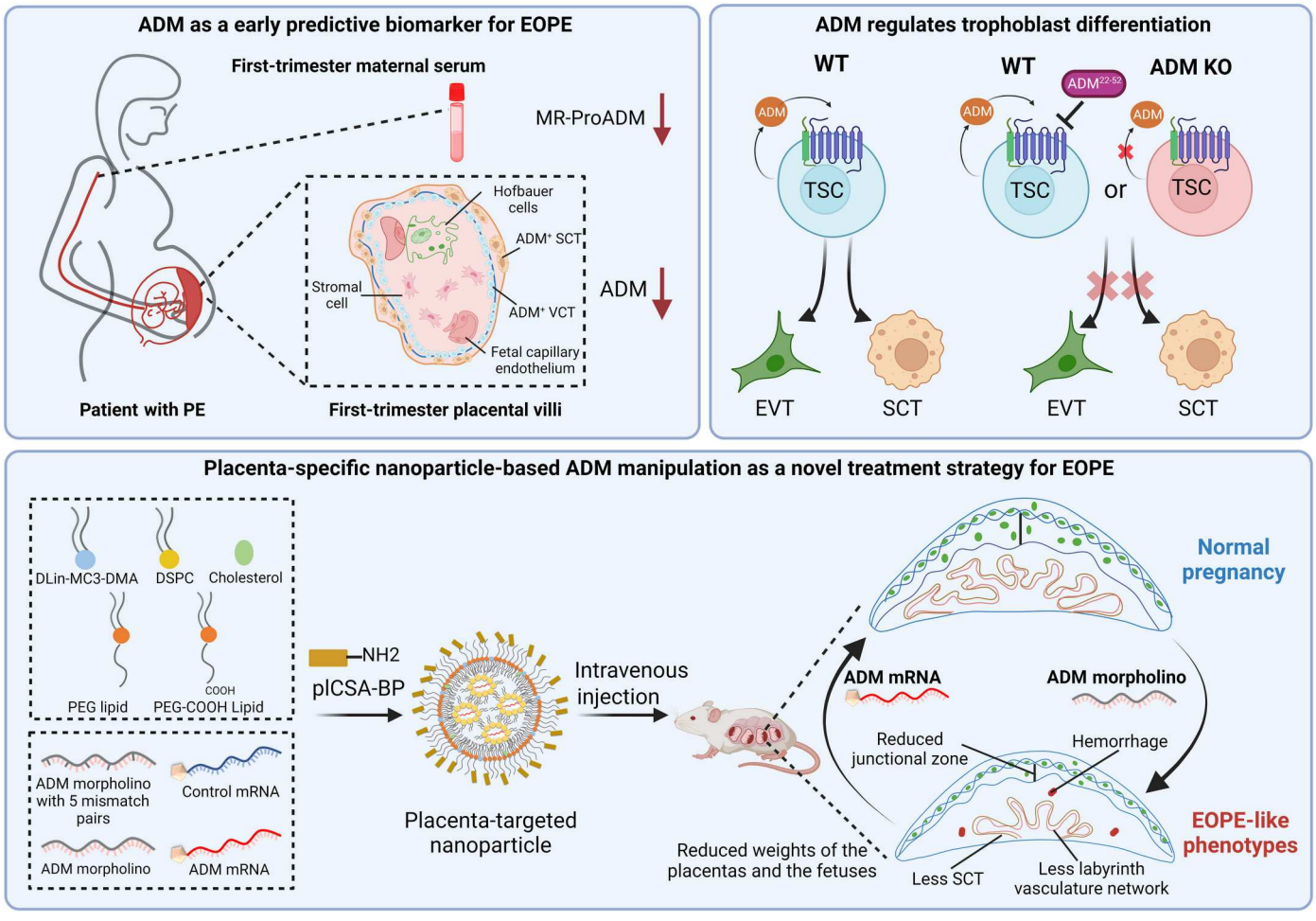

Fig. 8. The schematic diagram demonstrates the involvement of ADM in human placental development by regulating trophoblast differentiation. It also shows how a deficiency in placental ADM contributes to the development of EOPE. (**Top left**) ADM has the potential to serve as an early predictive biomarker for EOPE. (**Top right**) ADM is involved in the regulation of trophoblast differentiation. (**Bottom**) A potential new approach for treating EOPE may include manipulating the trophoblastic ADM expression by nanotechnology in repairing the developmental defect of EOPE trophoblasts.

First-trimester placental tissue (NP, n = 28; EOPE, n = 4) and maternal serum (NP, n = 80; EOPE, n = 8) surplus for diagnosis needed were obtained from patients undergoing diagnostic CVS procedure via a transabdominal approach at 11 to 13 + 6 weeks of gestation. Samples were flash-frozen in liquid nitrogen and then stored at −80°C until delivery. NP and EOPE term placentas (n = 6) were collected from the women who met the criteria of EOPE and underwent cesarean section. The tissues were collected and fixed in 4% formalin overnight, rinsed in phosphate-buffered saline (PBS), and transferred to 70% ethanol before standard processing to obtain paraffin-embedded sections (Histopathology Service, Department of Pathology, The University of Hong Kong).

Culture of human TSCs

Human TSC (hTSC) lines were established from hEPSCs as described (*27*). hTSCs were maintained on 1% Geltrex, cultured in a 37°C incubator, and enzymatically passaged (1:3) every 3 to 5 days by TrypLE. Cells were dissociated and centrifuged (300*g* for 3 min) in a 10% fetal bovine serum (FBS)–containing medium. After removing the supernatant, hTSC was resuspended and seeded in the TSC medium (TSCM). The TSCM is prepared by supplementing Dulbecco's modified Eagle's medium (DMEM)/F12 with 50.0 μM β-mercaptoethanol, 0.2% FBS, 0.5% penicillin-streptomycin-glutamine, 0.3% Bovine serum albumin (BSA), 1.0% Insulin-Transferrin-Selenium-Ethanolamine (ITS-X) supplement, L-ascorbic acid (50.0 μg/ml), epidermal growth factor (EGF; 50.0 ng/ml), 2.0 μM CHIR99021, 0.5 μM A83-01, 1.0 μM SB431542, 10.0 μM Valproic acid (VPA), and 5.0 μM Y27632.

Differentiation of hTSCs

hTSCs were grown to around 80% confluence in the TSCM and digested with TrypLE for 5 min at 37°C. For the induction of EVT-TSC, hTSC were seeded in a six-well plate precoated with 1% Matrigel at a density of 1×10^5 cells per well and cultured in 2 ml of EVT medium [DMEM/F12 supplemented with 50 μM β-mercaptoethanol, penicillin-streptomycin-glutamine, 0.3% BSA, 1% ITS-X, 7.5 μM A83-01, and 10 μM Y27632] supplemented with 4% KnockOut Serum Replacement (KSR), neuregulin 1 (NRG1) (100 ng/ml), and 2% Matrigel. On day 3, the media were replaced with 2 ml of EVT basal medium supplemented with 4% KSR and 0.5% Matrigel. On day 6, the media were replaced with 2 ml of EVT basal medium and 0.5% Matrigel. The cells were harvested for downstream analysis on day 8.

For the induction of SCT-TSC, hTSCs (2.0×10^5) were seeded in a six-well plate precoated with 1% Matrigel in 2 ml of SCT medium (DMEM/F12 supplemented with 50 μM β-mercaptoethanol, 0.5% penicillin-streptomycin-glutamine, 0.3% BSA, 1% ITS-X, 2.5 μM Y-27632, 2 μM forskolin, and 4% KnockOut Serum Replacement). The medium was changed on day 3, and the cells were harvested for downstream analysis on day 6.

Culture and differentiation of human trophoblast organoid

Human trophoblast organoids were derived from primary first-trimester placenta tissue as described (*31*, *70*) and cultured in Matrigel Matrix (Corning, USA) with organoid medium [DMEM/F12 supplemented with 0.5% penicillin-streptomycin, B27 supplement minus vitamin A, N2 supplement, 2 mM L-glutamine, 1.25 mM *N*-acetyl-L-cysteine, rspondin-1 (500 ng/ml), EGF (50 ng/ml), fibroblast growth factor 2 (100 ng/ml), HGF (50 ng/ml), 2 μM CHIR99021, 5 μM Y27632, 500 nM A83-01, 2.5 μM (Prostaglandin E2) PGE2, and Primocin (100 μg/ml)]. The organoids were anatomically and functionally resembling the villous composed of CT and SCT and could differentiate into EVT.

Trophoblast organoids were differentiated into EVT and SCT using the same medium and protocols as for hTSCs. To measure EVT differentiation, the organoids in Matrigel were dissolved in cell recovery solution, and the differentiated EVTs were obtained by filtering through a 40-μm cell strainer. To measure SCT differentiation, the β-hCG concentrations of the conditioned media were measured by an immunoassay analyzer (The Architect, i1000SR).

Animal experiments

All animal experiments were conducted under license from the Department of Health, Hong Kong Special Administrative Region (19-1588), in DH/HT&A/8/2/3Pt.4 and were approved by the Committee on the Use of Live Animals in Teaching and Research, The University of Hong Kong (CULATR 5317-20). CD1 mice (6 to 8 weeks of age) were caged in a specific pathogen–free animal room with a 14-hour light/10-hour dark cycle. Gestational ages were determined by monitoring the formation of vaginal plugs (counted as E0.5).

Noninvasive placenta-specific ADM suppression mouse model

Pregnant mice were injected intravenously with 100 μl of 10 μM nanoparticles on E5.5, E7.5, and E9.5 entrapping five-mispair ADM MO oligo (Control Mor-NPs group) and anti-ADM MO (ADM Mor-NPs group). Pregnant mice were euthanized at E11.5, E13.5, E15.5, and E17.5. The embryos and placentas were collected and weighed. The tissues were fixed with 4% paraformaldehyde (PFA) in PBS for paraffin sectioning.

PE mouse model and placenta-specific ADM overexpression in PE mouse model

L-NAME was administrated to induce the PE mouse model by intraperitoneal injection. Pregnant CD1 was injected with L-NAME (60 mg/kg per day; N5751, Sigma-Aldrich, St. Louis, MO, USA) daily from E5.5 to E13.5 as L-NAME group. Pregnant mice were divided into four groups: (i) vehicle control, (ii) L-NAME, (iii) L-NAME + nanoparticles entrapping CleanCap Firefly luciferase modified mRNA (mmRNA; control-MNPs), and (iv) L-NAME + nanoparticles entrapping Custom CleanCap ADM mmRNA (ADM-MNPs). L-NAME was administered daily from E5.5 to E13.5 of pregnancy and nanoparticles on E6.5, E8.5, E10.5, and E12.5. Pregnant mice were euthanized at E13.5, and the embryos and placentas were collected and weighed. The tissue was fixed by 4% PFA in PBS for paraffin sectioning.

Spatial transcriptomics and data analysis

Sample preparation

The human villi samples were collected by the termination of pregnancy because of psychosocial reasons at 6 to 8 weeks of gestation with written consent. The samples were fixed by 4% PFA overnight and then dehydrated in 10, 20, and 30% sucrose. The fresh mouse placentas or fixed human villi were embedded in precooled Tissue-Tek OCT (Sakura, 4583), snap-frozen in liquid nitrogen, and transferred to Beijing Genomics Institute (BGI)–Research for subsequent experiments. Cryosections were conducted at a thickness of 5 μm in a cryostat (DAKEWE Cryostat Microtome, 6250).

Stereo-seq libraries construction

Stereo-seq libraries were prepared and sequenced as previously described (*71*), while PFA-fixed samples were prepared with an extra decrosslinking procedure. The chips were immersed in TE buffer (pH = 10) with 5% ribonuclease inhibitor at 70°C for 1 hour and then fixed in precooled methanol to refix at −20°C for 15 min. Last, the captured RNAs were reverse-transcribed to cDNA. After amplification, fragmentation, and cyclization, the DNA nanoballs (DNBs) were sequenced on the MGI DNBSEQ-T1 sequencer according to the manufacturer's protocol (BGI, Shenzhen, China).

Stereo-seq data analysis

The raw data were processed as previously described (*71*, *72*) to generate expression profile matrices with coordinate identity (CID). Then, the expression profile matrices of sections were divided into bins with 50 × 50 DNBs. We selected regions with high-quality captured genes and relatively intact villi structures according to the hematoxylin and eosin (H&E) staining slides or single-stranded DNA (ssDNA) map. The selected data were further processed by Scanpy (*73*) through the pipeline of normalization, scaling, feature gene selection, principal components analysis dimension reduction, and clustering with a resolution parameter set to 0.4, and a list of marker genes for each cluster was generated. The clusters were annotated by acquiring the top 20 genes with the most significant *P* values to the published results. Clusters that could match the most marker genes to a specific cell type were assigned to that type of cell. To identify cell type abundances in each spatial spot, we conducted deconvolution analysis by *cell2location* (*74*). We use the scRNA-seq data by Vento-Tormo *et al.* (*23*) for the spatial data deconvolution.

Immunohistochemistry of the human term placental tissue

Immunohistochemistry of paraffin-embedded human term placental tissue sections (5 μm) was performed by monoclonal anti-ADM antibody (1:100; ab69117, Abcam, UK) or isotype control antibody. Nonspecific immunoglobulin binding sites were masked by a 1-hour incubation in 10% goat serum in PBS. Slides were incubated overnight at 4°C with primary antibodies followed by the biotinylated secondary antibody for 2 hours. Immunodetection was performed by VECTASTAIN Elite ABC kit (PK6100, Vector Laboratories) according to the manufacturer's instructions using 3,3′-diaminobenzidine tetrahydrochloride (Dako) as chromagen/substrate. The slides were counterstained with hematoxylin, mounted in Permount medium (SP15-500, Thermo Fisher Scientific), and observed under the light microscope (Zeiss).

Guide RNA design and plasmid DNA preparation

The human ADM exon 2 and exon 3 sequences were analyzed using the online CRISPOR tool for designing a pair of highly specific guide RNAs (gRNAs). Chemically synthesized ssDNA oligos were incubated at 95°C for 10 min for annealing into double-stranded DNA, which were then ligated into a linearized empty gRNA vector using the DNA Ligation Kit, Mighty Mix. The ligation product was transformed into Chemically Competent *E. coli* TOP10 cells (Tiangen, Beijing China) and spread onto an LB agar plate with ampicillin for selection. The next day, single colonies were picked and cultured in LB broth with ampicillin for plasmid miniprep using the TIANprep Rapid Mini Plasmid Kit. After confirmation of ligated gRNA sequences by Sanger Sequencing, gRNA plasmids with the correct target sequence were amplified and extracted by the EndoFree Plasmid Kit II to purify a large amount of endotoxin-free gRNA plasmid DNA for electroporation. Plasmid DNA of BSD-Cas9 was similarly prepared as described.

Electroporation and selection

Electroporation of hTSC was performed when the cells reached 70 to 80% confluence. Plasmid DNA including Cas9 and double sgRNA (single gRNA) at a ratio of 2:1:1 (6 μg of Cas9, 3 μg of sgRNA1, 3 μg of sgRNA2 per 1.0×10^6 cells as one group) was added into 100 μl of resuspension buffer R. hTSCs were washed twice with PBS and then dissociated into single cells using 0.05% trypsin-EDTA. M10 medium (DMEM with 10% FBS) was added to neutralize the trypsin. hTSCs were resuspended in the resuspension buffer R containing the plasmid DNA mixture. Electroporation was performed using the Neon Transfection System at 140 V, 30 ms, and 1 pulse. After electroporation, cells were seeded with a TSCM. After incubation overnight, cells were switched to a typical hTSC medium. One day after electroporation, cells were selected by Blasticidin S HCl (10 μg/ml) and puromycin dihydrochloride (1 μg/ml) for 3 days. After 7 to 10 days, single colonies were picked for expansion and genotyping.

Genotyping and Sanger sequencing

Single hTSC colonies were picked and digested into single cells in a 96-well plate using TrypLE for 3 to 5 min. Half of these cells were transferred into a 48-well plate with TSCM for culturing. The other half of cells of the same colony were collected for genotyping using primers designed to amplify the targeted and the wild-type bands. The genotyping primer sequences for ADM were as follows: forward, 5′-ACTCAGTGGTTTCTTGGTGACACTG-3′ and reverse, 5′-GTCAAGCGTACCGCCAGAGCATG-3′. The mutant polymerase chain reaction (PCR) band was gel-purified and confirmed by Sanger sequencing for a 338–base pair deletion.

Flow cytometry

Cell suspensions were first stained with Zombie Aqua Fixable Viability Kit for 20 min and washed one time with buffer containing serum. Then, cell surface staining was generated for 30 min at 4°C. The cells were permeabilized and followed by staining intracellular molecules. The labeled cells were thoroughly washed, and cell surface and intracellular molecular expressions were analyzed on CytoFLEX (Beckman Coulter, USA), with data analyzed using FlowJo version 10.1 software (Tree Star, Ashland, OR USA).

Transwell invasion assay

The invasion ability of hTSC-derived EVTs was determined by cell invasion according to the manufacturers' instructions. Briefly, the invasion chambers were incubated with warm DMEM base medium at 37°C for 1 hour. After rehydration, the medium was removed. TSC-EVTs (1×10^5 cells per well) were mixed with DMEM basal medium, and the mixture was added into an invasion chamber and placed into a 24-well culture plate, with the lower chamber filled with DMEM containing 10% FBS. The cells were allowed to pass through the chamber and attached to the lower bottom of the polycarbonate membrane for 22 hours. After that, the medium from the top insert was aspirated, and noninvasive/migratory cells on the upper surface were wiped away with a cotton bud. The invaded/migrated cells on the lower surface were stained

with crystal violet for 15 min. The membrane was observed under a light microscope.

Reverse transcription quantitative PCR

Total RNA was extracted using the QuickPrep RNA extraction kit (GE HealthCare), and reverse-transcribed using the TaqMan Reverse Transcription Reagent (Applied Biosystems). Quantitative PCR (qPCR) was conducted in a QuantStudio 5 Real-Time PCR System (Applied Biosystems) using TaqMan qPCR assay probes. The probes consisted of the pan-trophoblast marker, CK7 (KRT7, Hs00559840_m1); TSC marker, GATA3 (Hs00231122_m1) and TEA domain transcription factor 4 (TEAD4; Hs01125042_mH); EVT markers, HLA-G (Hs00365950_g1), matrix metallopeptidase 2 (MMP2; Hs01548727_m1), integrin subunit α 5 (ITGA5, Hs01547673_m1), and fibronectin 1 (FN1, Hs01549976_m1); and SCT markers, pregnancy-specific beta-1-glycoprotein 1 (PSG1, Hs04235345_s1), syndecan 1 (SDC1, Hs00174579_m1), and chorionic gonadotropin subunit β 3 (CGB3, Hs00361224_gH). 18*S* ribosomal RNA (Hs99999901_s1) was used as the internal control. The reactions were performed in triplicate. The threshold cycle (CT) method ($2^{-\triangle\triangle CT}$ method) was applied.

RNA-seq analysis

Total RNA from cultured TSC/TSC$^{ADM\ KO}$, D2 EVT^{TSC}/D2 EVT$^{ADM\ KO\ TSC}$, and D2 SCT^{TSC}/D2 SCT$^{ADM\ KO\ TSC}$ was extracted using TRIzol Reagent (15596018, Invitrogen) according to the instruction. mRNA was purified with Oligo(dT)-attached magnetic beads, followed by fragmentation. The first strand and second cDNA were generated by random hexamer-primed reverse transcription. The cDNA was amplified by PCR and purified by AMPure XP Beads. The quality control of the products was verified by Agilent Technologies 2100 Bioanalyzer. After generating cluster on flow cell, sequencing by synthesis technology was used to obtain the base-by-base genome information. For data analysis, we first used *fastp* (version 0.23.2) (*75*) to remove low-quality reads from raw data with default parameters. Then, high-quality reads were aligned to the *Homo sapiens* (human) genome assembly GRCh38 (hg38) with the gene annotation file by *HISAT2* (version 7.5.0) (*76*) using the parameters --no-mixed --no-discordant --qc-filter. Gene abundance was quantified by *featureCounts* (version 2.0.1) (*77*) with the default parameters. The gene-level read count matrix was then imported into the R (version 4.1.0) (*78*) for differential gene expression analysis. In this process, *DEseq2* (version 1.32.0) (*79*), *edgeR* (version 3.34.1) (*80*), *limma* (version 3.48.3) (*81*), and *DEGseq* (version 1.46.0) (*82*) packages were used. Differentially expressed genes from each package were further filtered to retain that with raw *P* value <0.05 and fold change contrast ≥2. The union of filtered differentially expressed genes from each packaged were used for functional enrichment with *clusterProfiler* (version 4.0.5) (*83*).

Morpholino oligonucleotides based on knockdown of ADM

Morpholino oligonucleotides were obtained from Gene Tools, LLC. (Corvalis, OR). The sequences of the morpholino oligonucleotide are as follows: anti-ADM MO and (5′TCAGGGTGATGGAAACCAGCTTCAT3′) and 5-mispair ADM MO oligo as control (5′TCTGCGTGATCGAAACGACCTTCAT3′).

mmRNA based on overexpression of ADM

Polyadenylated and capped mmRNAs were synthesized by TriLink (San Diego, CA) as follows: CleanCap Firefly luciferase mmRNA and Custom CleanCap ADM mmRNA (based on NM_009627.2): Atgaagctggtttccatcaccctgatgttattgggttcactcgctttcctaggcgcggacactg-cagggccagatactccttcgcagttccgaaagaagtggaataagtgggcgctaagtcgtgg-gaagagggaactacaagcatccagcagctaccctacgggactcgctgatgagacgacagttcc-tacccagactcttgatccattcctggacgagcagaacacaactggccccctacaagccagcaat-cagagcgaagcccacattcgtgtcaaacgctaccgccagagcatgaaccagggttcccgcag-caatggatgccgcttcgggacctgcacatttcagaaattggcccaccagatctaccagctaaca-gacaaagacaaggacggcatggctcccagaaacaagatcagccctcaaggc-tatggccgccggcgccggcgttccctgctggaggtcctccggtcccggactgtggagtcctcc-caggagcagacacacacagccccaggcccctgggcgcacatctccagactctttaggatatag.

Formulation of lipid nanoparticles

Lipid nanoparticles (LNPs) were prepared by synthesized using NanoAssemblr Ignite (Precision NanoSystem Inc.). Organic phase solution formulation is as follows: Total organic phase solution concentration was 12.5 mM including cationic lipid Dlin-MC3-DMA, DSPC, cholesterol, PEG2000-DMG, and PEG2000-COOH (48.8%:9.8%:36.6%:2.4%:2.4% ratio) in absolute ethanol. For the aqueous solution formulation, morpholino oligonucleotides and modified mRNA in DEPC water were used. The concentration is calculated when the organic phase is kept at 12.5 mM and the nitrogen-to-phosphorus ratio is 4:1. The organic phase solution and aqueous solution were injected into a microfluidic mixing device NanoAssemblr Ignite. The parameter flow ratio (C:R) is set to 3:1; the total volume is 11.20 ml, and the flow rate is 12 ml/min. The resultant mixture was ultrafiltrated against PBS (pH 7.4) by using an ultrafiltration tube (Amicon Ultra-4 Centrifugal Filter Units) at 2000*g* at room temperature for 30 min. All materials were prepared and handled under ribonuclease-free conditions throughout the synthesis, formulation, and characterization steps.

Synthesis of plCSA-BP-conjugated LNP

The specific targeting placenta of LNP in vivo was studied using placental chondroitin sulfate A–binding peptide (plCSA-BP)–coated LNP by an established mouse model (*33*). Placental CSA-binding peptide was purchased from China Peptides Co. Ltd. (Shanghai, China). Placental CSA-binding peptides were conjugated to the nanoparticle surface using the 1-ethyl-3-(3-dimethylaminopropyl) carbodiimide (EDC)/*N-hydroxysuccinimide* (NHS) technique (*84*). First, 1 mg of LNPs was suspended in 3 ml of 0.1 M MES buffer (pH 5.5). To preactivate the carboxylic group, 28.3 μg of EDC and 17 μg of NHS were mixed on a shaker for 15 min. Next, 0.5 mg of plCSA-BP in 500 μl of deionized water was added to the reaction mixture. Then, 250 μl of 20× PBS was added to buffer the reaction at pH 7.0 to 8.0. The reaction mixture was then stirred overnight. Excess peptides and other impurities, such as EDC and NHS, were removed by filtration thrice using the AmiconUltra-4 centrifugal filters (molecular mass, 10 kDa; Millipore, MA, USA).

Characterization of the nanoparticles

The size, number, and zeta potential of nanoparticles were measured by ZetaView BASIC PMX 220 ZetaView TWIN Laser (Particle Metrix, Meerbusch, Germany) and analyzed by the corresponding software ZetaView version 8.05.11. Nanoparticles were diluted with particle-free water (1:1000), and a total volume of 500-μl samples was injected into the cell assembly without air

bubbles. A total of 11 positions were recorded and analyzed. The 100-nm polystyrene particles were used in the ZetaView system as alignment control. The temperature was maintained at around 27° C. The zeta potential of nanoparticles was measured by detecting the electrophoretic mobility of nanoparticle migration in an electric field. The zeta potential symmetry correction was performed, followed by the zeta potential analysis.

The shape of nanoparticles was observed by transmission electron microscopy (TEM; Philips CM100; Electron Microscope Unit, The University of Hong Kong). Nanoparticles were diluted with ultrapure water (100-fold dilution), placed on an electron microscopy grid, and allowed to incubate for 5 min. Then, the grid was stained by 100 μl of 2% (w/v) phosphotungstic for 2 min. The TEM grid was washed with ultrapure water and semidried. The images of nanoparticles were captured, and the diameter was quantified under the TEM.

Quant-iT RiboGreen RNA assay (Life Technologies, CA, USA) was used to quantify mmRNA encapsulation of nanoparticles after conjugation. Nanoparticles or dilutions of mmRNA at known concentrations were diluted in a final volume of 100 μl of TE buffer (10 mM tris-HCl and 20 mM EDTA) with or without 1% Triton X-100 (Sigma-Aldrich) in a 96-well fluorescent plate (Costar, Corning, NY, USA). The plate was incubated for 10 min at 40°C to permeabilize the particles before adding 99 μl of TE buffer and 1 μl of RiboGreen reagent to each well. Plates were shaken for 5 min, and the fluorescence intensity (excitation, 485 nm; emission, 528 nm) was measured using a plate reader (Biotek).

Noninvasively measuring mouse blood pressure

The blood pressure of pregnant female mice at different stages of gestation, specifically on E5.5, E7.5, E9.5, E11.5, E13.5, E15.5, and E17.5, was assessed noninvasively using the BP-2000 blood pressure analysis system (BIOSEB). The measurement was carried out by encircling the tail of the mice with a detector and using transmission photoplethysmography to determine the blood pressure as described.

Immunofluorescence staining of the human first-trimester placental tissue and mouse placenta

To examine the localization and expression of ADM, human first trimester CVS samples were processed in frozen sections (5 μm), fixed by 4% PFA, and then permeabilized by eBioscience Permeabilization Buffer (00-8333-56, Thermo Fisher Scientific, MA, USA) for 15 min. Slides were blocked in 10% goat serum and then stained with monoclonal anti-ADM antibody (1:100; ab69117, Abcam, UK) or anti-rabbit immunoglobulin G (IgG) isotype control antibody (1:100; ab172730, Abcam), followed by Alexa Fluor 488–conjugated goat anti-rabbit antibody (1:500; A11070, Invitrogen, USA). Nuclei were stained with DAPI (4′,6-diamidino-2-phenylindole; 1:500, Invitrogen). The slides were mounted with a mounting medium (S3023, Dako, Glostrup, Denmark) and observed under a Zeiss Laser scanning confocal microscope (LSM 980, Zeiss, Carl, Faculty Core Facility of Li Ka Shing Faculty of Medicine Faculty, The Hong Kong University).

To determine the structural defects in the placenta, mouse placenta sections were stained for (i) E-cadherin (Cdh1) to demarcate the labyrinthine SCT (*26*, *27*), (ii) MCT1 to label the SCT I (*57*, *85*), (iii) MCT4 to label the SCT II (*57*, *85*), (iv) TPBPA to label the spongiotrophoblast and glycogen cells, (v) CK7 as a pan trophoblast maker (*57*, *85*), (vi) laminin to highlight the basement membrane, and (vii) ADM to detect ADM expression.

For immunostaining, antigen retrieval of the deparaffinized sections was performed by heating in Target Retrieval Solution (S1699, Dako). The sections were permeabilized by eBioscience Permeabilization Buffer (00-8333-56, Thermo Fisher Scientific, MA, USA), followed by blocking in 1% BSA/PBS. The sections were incubated with primary antibodies overnight in the cold room. Primary antibodies were detected with appropriate fluorescence or horseradish peroxidase–conjugated secondary antibodies. Nuclei were counterstained with hematoxylin or DAPI.

Quantification of fluorescent intensity was performed with ImageJ software using images acquired at identical illumination settings following previously described protocols (*86*). Briefly, the images are acquired with a Nikon eclipse Ti (Nikon Instruments Inc., Japan) equipped with an objective at 20× to generate the image size of 1600 × 1200 pixels. The signal intensity of the whole image was then measured as integrated density (fluorescence area × mean fluorescence intensity) of an image-adjust-threshold monochrome image and was calculated using the following equation: Fluorescence intensity = integrated density of selected area − integrated density of background. This information has been added in the revised manuscript.

Histology of mouse placenta

Mouse placentas were weighed after removing the umbilical cord and fetal membranes. Consecutive 5-μm sections of mouse placentas were produced and processed for H&E staining by a standard protocol. Sections were incubated in Mayer′s Hematoxylin (51275, Sigma-Aldrich) for 5 min and briefly washed in tap water. Sections were subsequently differentiated in 70% acid alcohol (70% ethanol and 1% hydrochloric acid) for 10 s, incubated in cold tap water for 30 min, and incubated in eosin (HT110116, Sigma-Aldrich) for 30 s, followed by an increasing ethanol row (70% for 3 min, 95% for 3 min, 100% for 3 min, and 100% for 3 min). After that, the sections were incubated in 100% xylene for 5 min before mounting with Eukitt quick-hardening mounting medium (03989, Sigma-Aldrich). The placenta sections through the sagittal midline were chosen for imaging by light microscopy.

Enzyme-linked immunosorbent assay

Human and mouse serum samples were collected from anticoagulant blood and centrifuged at 1000*g* for 20 min within 30 min of collection. The samples were stored at −80°C until detection. Plasma was fourfold diluted, and the level of human MR-proADM and mouse ADM were quantified by ELISA kits [MR pro-ADM (Human) ELISA Kit: EKE61390, Biomatik; Mouse ADM ELISA Kit: EKE61865, Biomatik] following the manufacturer′s instructions.

Estimation of proteinuria

Mice were placed individually in a metabolic cage to collect urine from E10.5 to E13.5. Mouse albumin (ab108792, Abcam) and creatinine (ab65340, Abcam) were measured according to the manufacturer′s instructions.

Western blot

Extraction of proteins from the whole-cell lysate and tissues was performed with radioimmunoprecipitation assay lysis and

extraction buffer (89900, Thermo Fisher Scientific) containing 1% proteinase inhibitor cocktail (11836170001, Roche) and 1% phosphatase inhibitor cocktail (5870, Cell Signaling Technology) followed by centrifugation at 12,000 rpm and 4°C for 30 min. Protein concentrations of the supernatants were quantified by using the BCA Protein Assay Kit (23225, Thermo Fisher Scientific). Protein samples were separated by SDS–polyacrylamide gel electrophoresis gels and transferred to polyvinylidene difluoride membranes, followed by overnight incubation with primary antibodies including anti-ADM (1:1000; TA806874, OriGene), anti–phospho-PI3K p85/p55 (1:1000; 17366, Cell Signaling Technology), anti–phospho-Akt (Ser^{473}) (1:2000; 4060, Cell Signaling Technology), anti-PI3K p110α (1:1000; 4255, Cell Signaling Technology), and anti-Akt (1:1000; 4691, Cell Signaling Technology) at 4°C. Bands were then washed with 0.1% Tween 20 in tris-buffered saline and incubated with goat anti-rabbit/mouse IgG antibody (horseradish peroxidase) (NA934/NA931, Cytiva) for 1 hour at room temperature. Then, the bands were detected using Signal Fire Elite ECL Reagent (12757, Cell Signaling Technology).

Statistical analysis

All the experimental data were expressed as means ± SD. Two-tailed unpaired Student *t* test, one-way analysis of variance (ANOVA) with Tukey's post hoc test, Newman-Keuls, multiple comparisons test, and two-way ANOVA with Tukey's multiple comparisons tests were conducted using GraphPad Prism 9 (GraphPad Software Inc., USA). A probability value of <0.05 was considered statistically significant.

Supplementary Materials

This PDF file includes:

Figs. S1 to S7

Tables S1 and S2

REFERENCES AND NOTES

1. B. W. Mol, C. T. Roberts, S. Thangaratinam, L. A. Magee, C. J. De Groot, G. J. Hofmeyr, Pre-eclampsia. *Lancet* **387**, 999–1011 (2016).
2. M. Y. Turco, A. Moffett, Development of the human placenta. *Development* **146**, dev163428 (2019).
3. N. M. Gude, C. T. Roberts, B. Kalionis, R. G. King, Growth and function of the normal human placenta. *Thromb. Res.* **114**, 397–407 (2004).
4. L. C. Chappell, C. A. Cluver, J. Kingdom, S. Tong, Pre-eclampsia. *Lancet* **398**, 341–354 (2021).
5. O. Farah, C. Nguyen, C. Tekkatte, M. M. Parast, Trophoblast lineage-specific differentiation and associated alterations in preeclampsia and fetal growth restriction. *Placenta* **102**, 4–9 (2020).
6. S. Rana, E. Lemoine, J. P. Granger, S. A. Karumanchi, Preeclampsia: Pathophysiology, challenges, and perspectives. *Circ. Res.* **124**, 1094–1112 (2019).
7. C. Catarino, I. Rebelo, L. Belo, A. Quintanilha, A. Santos-Silva, Umbilical cord blood changes in neonates from a preeclamptic pregnancy. *Fr. Preconc. Postp.* **12**, 269–287 (2012).
8. P. Gathiram, J. Moodley, Pre-eclampsia: Its pathogenesis and pathophysiolgy: review articles. *Cardiovasc. J. Afr.* **27**, 71–78 (2016).
9. H. Valensise, B. Vasapollo, G. Gagliardi, G. P. Novelli, Early and late preeclampsia. *Hypertension* **52**, 873–880 (2008).
10. R. Thadhani, E. Lemoine, S. Rana, M. M. Costantine, V. F. Calsavara, K. Boggess, B. J. Wylie, T. A. M. Simas, J. M. Louis, J. Espinoza, S. L. Gaw, A. Murtha, S. Wiegand, Y. Gollin, D. Singh, R. M. Silver, D. E. Durie, B. Panda, E. R. Norwitz, I. Burd, B. Plunkett, R. K. Scott, A. Gaden, M. Bautista, Y. Chang, M. A. Diniz, S. A. Karumanchi, S. Kilpatrick, Circulating angiogenic factor levels in hypertensive disorders of pregnancy. *NEJM Evid.* **1**, 2200161 (2022).
11. H. Zeisler, E. Llurba, F. Chantraine, M. Vatish; A. C. Staff, M. Sennström, M. Olovsson, S. P. Brennecke, H. Stepan, D. Allegranza, P. Dilba, M. Schoedl, M. Hund, S. Verlohren, Predictive value of the sFlt-1:PlGF ratio in women with suspected preeclampsia. *New Engl. J. Med.* **374**, 13–22 (2016).
12. M. Matin, M. Mörgelin, J. Stetefeld, B. Schermer, P. T. Brinkkoetter, T. Benzing, M. Koch, H. Hagmann, Affinity-enhanced multimeric VEGF (vascular endothelial growth factor) and PlGF (placental growth factor) variants for specific adsorption of sFlt-1 to restore angiogenic balance in preeclampsia. *Hypertension* **76**, 1176–1184 (2020).
13. U. D. Anderson, M. Olsson, K. Kristensen, B. Åkerström, S. Hansson, Review: Biochemical markers to predict preeclampsia. *Placenta* **33**, S42–S47 (2012).
14. L. K. Wagner, Diagnosis and management of preeclampsia. *Am. Fam. Physician* **70**, 2317–2324 (2004).
15. P. M. Lenhart, K. M. Caron, Adrenomedullin and pregnancy: Perspectives from animal models to humans. *Trends Endocrinol. Metabol.* **23**, 524–532 (2012).
16. K. Kobayashi, T. Kubota, T. Aso, Y. Hirata, T. Imai, F. Marumo, Immunoreactive adrenomedullin (AM) concentration in maternal plasma during human pregnancy and AM expression in placenta. *Eur. J. Endocrinol.* **142**, 683–687 (2000).
17. R. Di Iorio, E. Marinoni, C. Letizia, E. V. Cosmi, Adrenomedullin in perinatal medicine. *Regul. Pept.* **112**, 103–113 (2003).
18. M. Garayoa, E. Bodegas, F. Cuttitta, L. M. Montuenga, Adrenomedullin in mammalian embryogenesis. *Microsc. Res. Tech.* **57**, 40–54 (2002).
19. M. Li, D. Yee, T. R. Magnuson, O. Smithies, K. M. Caron, Reduced maternal expression of adrenomedullin disrupts fertility, placentation, and fetal growth in mice. *J. Clin. Invest.* **116**, 2653–2662 (2006).
20. K. Padma, G. L. Deepika, P. Josthna, Infusion of adrenomedullin 22-52 antagonist causes uteroimplantation growth restriction during early gestation in rats. *Drug Inven. Today* **9**, 28–34 (2017).
21. M. Li, N. M. Schwerbrock, P. M. Lenhart, K. L. Fritz-Six, M. Kadmiel, K. S. Christine, D. M. Kraus, S. T. Espenschied, H. H. Willcockson, C. P. Mack, K. M. Caron, Fetal-derived adrenomedullin mediates the innate immune milieu of the placenta. *J. Clin. Invest.* **123**, 2408–2420 (2013).
22. X. Han, Z. Zhou, L. Fei, H. Sun, R. Wang, Y. Chen, H. Chen, J. Wang, H. Tang, W. Ge, Y. Zhou, F. Ye, M. Jiang, J. Wu, Y. Xiao, X. Jia, T. Zhang, X. Ma, Q. Zhang, X. Bai, S. Lai, C. Yu, L. Zhu, R. Lin, Y. Gao, M. Wang, Y. Wu, J. Zhang, R. Zhan, S. Zhu, H. Hu, C. Wang, M. Chen, H. Huang, T. Liang, J. Chen, W. Wang, D. Zhang, G. Guo, Construction of a human cell landscape at single-cell level. *Nature* **581**, 303–309 (2020).
23. R. Vento-Tormo, M. Efremova, R. A. Botting, M. Y. Turco, M. Vento-Tormo, K. B. Meyer, J. E. Park, E. Stephenson, K. Polański, A. Goncalves, L. Gardner, S. Holmqvist, J. Henriksson, A. Zou, A. M. Sharkey, B. Millar, B. Innes, L. Wood, A. Wilbrey-Clark, R. P. Payne, M. A. Ivarsson, S. Lisgo, A. Filby, D. H. Rowitch, J. N. Bulmer, G. J. Wright, M. J. T. Stubbington, M. Haniffa, A. Moffett, S. A. Teichmann, Single-cell reconstruction of the early maternal-fetal interface in humans. *Nature* **563**, 347–353 (2018).
24. M. Langbein, R. Strick, P. L. Strissel, N. Vogt, H. Parsch, M. W. Beckmann, R. L. Schild, Impaired cytotrophoblast cell–cell fusion is associated with reduced Syncytin and increased apoptosis in patients with placental dysfunction. *Mol. Reprod. Develop.: Incorp. Gamete Res.* **75**, 175–183 (2008).
25. J. Xu, T. Sivasubramaniyam, Y. Yinon, A. Tagliaferro, J. Ray, O. Nevo, M. Post, I. Caniggia, Aberrant TGFβ signaling contributes to altered trophoblast differentiation in preeclampsia. *Endocrinology* **157**, 883–899 (2016).
26. L. Woods, V. Perez-Garcia, M. Hemberger, Regulation of placental development and its impact on fetal growth-new insights from mouse models. *Front. Endocrinol.* **9**, 570 (2018).
27. X. Gao, M. Nowak-Imialek, X. Chen, D. Chen, D. Herrmann, D. Ruan, A. C. H. Chen, M. A. Eckersley-Maslin, S. Ahmad, Y. L. Lee, T. Kobayashi, D. Ryan, J. Zhong, J. Zhu, J. Wu, G. Lan, S. Petkov, J. Yang, L. Antunes, L. S. Campos, B. Fu, S. Wang, Y. Yong, X. Wang, S.-G. Xue, L. Ge, Z. Liu, Y. Huang, T. Nie, P. Li, D. Wu, D. Pei, Y. Zhang, L. Lu, F. Yang, S. J. Kimber, W. Reik, X. Zou, Z. Shang, L. Lai, A. Surani, P. P. L. Tam, A. Ahmed, W. S. B. Yeung, S. A. Teichmann, H. Niemann, P. Liu, Establishment of porcine and human expanded potential stem cells. *Nat. Cell Biol.* **21**, 687–699 (2019).
28. H. Okae, H. Toh, T. Sato, H. Hiura, S. Takahashi, K. Shirane, Y. Kabayama, M. Suyama, H. Sasaki, T. Arima, Derivation of human trophoblast stem cells. *Cell Stem Cell* **22**, 50–63 (2018).
29. M. Nowak-Imialek, X. Gao, P. Liu, H. Niemann, 182 establishment of expanded potential embryonic stem cell lines from porcine embryos. *Reprod. Fertil. Dev.* **31**, 215–216 (2019).
30. D. Ruan, Z. W. Ye, S. Yuan, Z. Li, W. Zhang, C. P. Ong, K. Tang, T. T. Ka Ki Tam, J. Guo, Y. Xuan, Y. Huang, Q. Zhang, C. L. Lee, L. Lu, P. C. H. Chiu, W. S. B. Yeung, F. Liu, D. Y. Jin, P. Liu, Human early syncytiotrophoblasts are highly susceptible to SARS-CoV-2 infection. *Cell Rep. Med.* **3**, 100849 (2022).
31. C. L. Lee, Z. Chen, Q. Zhang, Y. Guo, V. W. Y. Ng, B. Zhang, K. Bai, D. Ruan, A. S. Y. Kan, K. W. Cheung, A. S. L. Mak, W. S. B. Yeung, R. Su, Q. Yang, M. Chen, M. R. Du, Z. Jian, X. Fan, P. C. N. Chiu, Dysregulation of the CD147 complex confers defective placental development: A pathogenesis of early-onset preeclampsia. *Clin. Transl. Med.* **12**, e826 (2022).

32. B. Zhang, L. Tan, Y. Yu, B. Wang, Z. Chen, J. Han, M. Li, J. Chen, T. Xiao, B. K. Ambati, L. Cai, Q. Yang, N. R. Nayak, J. Zhang, X. Fan, Placenta-specific drug delivery by trophoblast-targeted nanoparticles in mice. *Theranostics* **8**, 2765–2781 (2018).
33. B. Zhang, Z. Chen, J. Han, M. Li, N. R. Nayak, X. Fan, Comprehensive evaluation of the effectiveness and safety of placenta-targeted drug delivery using three complementary methods. *J Vis Exp* **1**, e58219 (2018).
34. E. Marinoni, K. Pacioni, A. Sambuchini, M. Moscarini, C. Letizia, R. D. Iorio, Regulation by hypoxia of adrenomedullin output and expression in human trophoblast cells. *Eur. J. Obstet. Gynecol. Reprod. Biol.* **154**, 146–150 (2011).
35. V. Faure-Bardon, J. Fourgeaud, T. Guilleminot, J. F. Magny, L. Salomon, J. P. Bernard, M. Leruez-Ville, Y. Ville, First-trimester diagnosis of congenital cytomegalovirus infection after maternal primary infection in early pregnancy: Feasibility study of viral genome amplification by PCR on chorionic villi obtained by CVS. *Ultrasound Obstet. Gynecol.* **57**, 568–572 (2021).
36. R. L. Hannibal, M. Cardoso-Moreira, S. P. Chetty, J. Lau, Z. Qi, E. Gonzalez-Maldonado, A. M. Cherry, J. Yu, M. E. Norton, J. C. Baker, Investigating human placentation and pregnancy using first trimester chorionic villi. *Placenta* **65**, 65–75 (2018).
37. A. Farina, A. Sekizawa, P. De Sanctis, Y. Purwosunu, T. Okai, D. H. Cha, J. H. Kang, C. Vicenzi, A. Tempesta, N. Wibowo, Gene expression in chorionic villous samples at 11 weeks' gestation from women destined to develop preeclampsia. *Prenat. Diagn.* **28**, 956–961 (2008).
38. J. D. Aplin, P. T. Ruane, Embryo–epithelium interactions during implantation at a glance. *J. Cell Sci.* **130**, 15–22 (2017).
39. P. T. Ruane, T. Garner, L. Parsons, P. A. Babbington, I. Wangsaputra, S. J. Kimber, A. Stevens, M. Westwood, D. R. Brison, J. D. Aplin, Trophectoderm differentiation to invasive syncytiotrophoblast is promoted by endometrial epithelial cells during human embryo implantation. *Hum. Reprod.* **37**, 777–792 (2022).
40. P. Merviel, L. Carbillon, J.-C. Challier, M. Rabreau, M. Beaufils, S. Uzan, Pathophysiology of preeclampsia: links with implantation disorders. *Eur. J. Obstet. Gynecol. Reprod. Biol.* **115**, 134–147 (2004).
41. J. Sehring, A. Beltsos, R. Jeelani, Human implantation: The complex interplay between endometrial receptivity, inflammation, and the microbiome. *Placenta* **117**, 179–186 (2022).
42. N. Minamino, K. Kikumoto, Y. Isumi, Regulation of adrenomedullin expression and release. *Microsc. Res. Tech.* **57**, 28–39 (2002).
43. N. G. Morgenthaler, J. Struck, C. Alonso, A. Bergmann, Measurement of midregional proadrenomedullin in plasma with an immunoluminometric assay. *Clin. Chem.* **51**, 1823–1829 (2005).
44. M. Christ-Crain, N. G. Morgenthaler, J. Struck, S. Harbarth, A. Bergmann, B. Müller, Mid-regional pro-adrenomedullin as a prognostic marker in sepsis: An observational study. *Crit. Care* **9**, 1–9 (2005).
45. J. Gille, H. Ostermann, A. Dragu, A. Sablotzki, MR-proADM: A new biomarker for early diagnosis of sepsis in burned patients. *J. Burn Care Res.* **38**, 290–298 (2017).
46. H. K. Gaggin, J. L. Januzzi Jr., Biomarkers and diagnostics in heart failure. *Biochim. Biophys. Acta* **1832**, 2442–2450 (2013).
47. J. Pedowska-Włoszek, M. Kostrubiec, K. Kurnicka, M. Ciurzynski, P. Palczewski, P. Pruszczyk, Midregional proadrenomedullin (MR-proADM) in the risk stratification of patients with acute pulmonary embolism. *Thromb. Res.* **132**, 506–510 (2013).
48. L. C. Poon, H. D. McIntyre, J. A. Hyett, E. B. da Fonseca, M. Hod, The first-trimester of pregnancy—A window of opportunity for prediction and prevention of pregnancy complications and future life. *Diabetes Res. Clin. Pract.* **145**, 20–30 (2018).
49. W.-Z. Lou, F. Jiang, J. Hu, X.-X. Chen, Y.-N. Song, X.-Y. Zhou, J.-T. Liu, X.-M. Bian, J.-S. Gao, Maternal serum angiogenic factor sFlt-1 to PlGF ratio in preeclampsia: A useful marker for differential diagnosis and prognosis evaluation in Chinese women. *Dis. Markers* **2019**, 1–7 (2019).
50. J. Sonek, D. Krantz, J. Carmichael, C. Downing, K. Jessup, Z. Haidar, S. Ho, T. Hallahan, H. J. Kliman, D. McKenna, First-trimester screening for early and late preeclampsia using maternal characteristics, biomarkers, and estimated placental volume. *Am. J. Obstet. Gynecol.* **218**, 126.e1–126.e13 (2018).
51. T. M. MacDonald, S. P. Walker, N. J. Hannan, S. Tong, J. Tu'uhevaha, Clinical tools and biomarkers to predict preeclampsia. *EBioMedicine* **75**, 103780 (2022).
52. R. J. Levine, S. E. Maynard, C. Qian, K.-H. Lim, L. J. England, K. F. Yu, E. F. Schisterman, R. Thadhani, B. P. Sachs, F. H. Epstein, Circulating angiogenic factors and the risk of preeclampsia. *New Engl. J. Med.* **350**, 672–683 (2004).
53. A. M. Carter, Animal models of human placentation–A review. *Placenta* **28**, S41–S47 (2007).
54. S. Panja, B. C. Paria, Development of the mouse placenta. *Adv. Anat. Embryol. Cell Biol.* **234**, 205–221 (2021).
55. N. de Alwis, N. K. Binder, S. Beard, Y. T. Mangwiro, E. Kadife, J. S. Cuffe, E. Keenan, B. R. Fato, J. Tu'uhevaha, F. C. Brownfoot, The L-NAME mouse model of preeclampsia and impact to long-term maternal cardiovascular health. *Life Sci. Alli.* **5**, e202201517 (2022).
56. K. L. Fritz-Six, W. P. Dunworth, M. Li, K. M. Caron, Adrenomedullin signaling is necessary for murine lymphatic vascular development. *J. Clin. Invest.* **118**, 40–50 (2008).
57. V. Perez-Garcia, E. Fineberg, R. Wilson, A. Murray, C. I. Mazzeo, C. Tudor, A. Sienerth, J. K. White, E. Tuck, E. J. Ryder, D. Gleeson, E. Siragher, H. Wardle-Jones, N. Staudt, N. Wali, J. Collins, S. Geyer, E. M. Busch-Nentwich, A. Galli, J. C. Smith, E. Robertson, D. J. Adams, W. J. Weninger, T. Mohun, M. Hemberger, Placentation defects are highly prevalent in embryonic lethal mouse mutants. *Nature* **555**, 463–468 (2018).
58. V. Chenouard, S. Remy, L. Tesson, S. Ménoret, L.-H. Ouisse, Y. Cherifi, I. Anegon, Advances in genome editing and application to the generation of genetically modified rat models. *Front. Genet.* **12**, 615491 (2021).
59. A. Dupressoir, C. Vernochet, O. Bawa, F. Harper, G. Pierron, P. Opolon, T. Heidmann, Syncytin-A knockout mice demonstrate the critical role in placentation of a fusogenic, endogenous retrovirus-derived, envelope gene. *Proc. Natl. Acad. Sci.* **106**, 12127–12132 (2009).
60. A. Dupressoir, C. Vernochet, F. Harper, J. Guégan, P. Dessen, G. Pierron, T. Heidmann, A pair of co-opted retroviral envelope syncytin genes is required for formation of the two-layered murine placental syncytiotrophoblast. *Proc. Natl. Acad. Sci.* **108**, E1164–E1173 (2011).
61. I. M. Larrayoz, L. Ochoa-Callejero, J. García-Sanmartín, C. Vicario-Abejón, A. Martínez, Role of adrenomedullin in the growth and differentiation of stem and progenitor cells. *Int. Rev. Cell Mol. Biol.* **297**, 175–234 (2012).
62. L. N. Kent, T. Konno, M. J. Soares, Phosphatidylinositol 3 kinase modulation of trophoblast cell differentiation. *BMC Dev. Biol.* **10**, 1–18 (2010).
63. H.-R. Kohan-Ghadr, B. Armistead, M. Berg, S. Drewlo, Irisin protects the human placenta from oxidative stress and apoptosis via activation of the Akt signaling pathway. *Int. J. Mol. Sci.* **22**, 11229 (2021).
64. D. Chakraborty, M. A. K. Rumi, T. Konno, M. J. Soares, Natural killer cells direct hemochorial placentation by regulating hypoxia-inducible factor dependent trophoblast lineage decisions. *Proc. Natl. Acad. Sci.* **108**, 16295–16300 (2011).
65. S. Qin, X. Tang, Y. Chen, K. Chen, N. Fan, W. Xiao, Q. Zheng, G. Li, Y. Teng, M. Wu, mRNA-based therapeutics: Powerful and versatile tools to combat diseases. *Signal Transduct. Target. Ther.* **7**, 1–35 (2022).
66. N. Veiga, M. Goldsmith, Y. Granot, D. Rosenblum, N. Dammes, R. Kedmi, S. Ramishetti, D. Peer, Cell specific delivery of modified mRNA expressing therapeutic proteins to leukocytes. *Nat. Commun.* **9**, 1–9 (2018).
67. Y. Yu, H. Jiang, L. Li, D. Zhu, X. Zhou, Q. Zhou, L. Sun, A Review of nanotechnology for treating dysfunctional placenta. *Front. Bioeng. Biotechnol.* **10**, (2022).
68. N. Pritchard, T. U. Kaitu'u-Lino, L. Harris, S. Tong, N. Hannan, Nanoparticles in pregnancy: The next frontier in reproductive therapeutics. *Hum. Reprod. Update* **27**, 280–304 (2021).
69. M. J. Mitchell, M. M. Billingsley, R. M. Haley, M. E. Wechsler, N. A. Peppas, R. Langer, Engineering precision nanoparticles for drug delivery. *Nat. Rev. Drug Discov.* **20**, 101–124 (2021).
70. M. Y. Turco, L. Gardner, R. G. Kay, R. S. Hamilton, M. Prater, M. S. Hollinshead, A. McWhinnie, L. Esposito, R. Fernando, H. Skelton, Trophoblast organoids as a model for maternal–fetal interactions during human placentation. *Nature* **564**, 263–267 (2018).
71. A. Chen, S. Liao, M. Cheng, K. Ma, L. Wu, Y. Lai, X. Qiu, J. Yang, J. Xu, S. Hao, X. Wang, H. Lu, X. Chen, X. Liu, X. Huang, Z. Li, Y. Hong, Y. Jiang, J. Peng, S. Liu, M. Shen, C. Liu, Q. Li, Y. Yuan, X. Wei, H. Zheng, W. Feng, Z. Wang, Y. Liu, Z. Wang, Y. Yang, H. Xiang, L. Han, B. Qin, P. Guo, G. Lai, P. Muñoz-Cánoves, P. H. Maxwell, J. P. Thiery, Q.-F. Wu, F. Zhao, B. Chen, M. Li, X. Dai, S. Wang, H. Kuang, J. Hui, L. Wang, J.-F. Fei, O. Wang, X. Wei, H. Lu, B. Wang, S. Liu, Y. Gu, M. Ni, W. Zhang, F. Mu, Y. Yin, H. Yang, M. Lisby, R. J. Cornall, J. Mulder, M. Uhlén, M. A. Esteban, Y. Li, L. Liu, X. Xu, J. Wang, Spatiotemporal transcriptomic atlas of mouse organogenesis using DNA nanoball-patterned arrays. *Cell* **185**, 1777–1792.e21 (2022).
72. M. Wang, Q. Hu, T. Lv, Y. Wang, Q. Lan, R. Xiang, Z. Tu, Y. Wei, K. Han, C. Shi, High-resolution 3D spatiotemporal transcriptomic maps of developing Drosophila embryos and larvae. *Dev. Cell* **57**, 1271–1283.e4 (2022).
73. F. A. Wolf, P. Angerer, F. J. Theis, SCANPY: Large-scale single-cell gene expression data analysis. *Genome Biol.* **19**, 15 (2018).
74. V. Kleshchevnikov, A. Shmatko, E. Dann, A. Aivazidis, H. W. King, T. Li, R. Elmentaite, A. Lomakin, V. Kedlian, A. Gayoso, M. S. Jain, J. S. Park, L. Ramona, E. Tuck, A. Arutyunyan, R. Vento-Tormo, M. Gerstung, L. James, O. Stegle, O. A. Bayraktar, Cell2location maps fine-grained cell types in spatial transcriptomics. *Nat. Biotechnol.* **40**, 661–671 (2022).
75. S. Chen, Y. Zhou, Y. Chen, J. Gu, fastp: An ultra-fast all-in-one FASTQ preprocessor. *Bioinformatics* **34**, i884–i890 (2018).
76. D. Kim, J. M. Paggi, C. Park, C. Bennett, S. L. Salzberg, Graph-based genome alignment and genotyping with HISAT2 and HISAT-genotype. *Nat. Biotechnol.* **37**, 907–915 (2019).

77. Y. Liao, G. K. Smyth, W. Shi, featureCounts: An efficient general purpose program for assigning sequence reads to genomic features. *Bioinformatics* **30**, 923–930 (2014).
78. R. C. Team, *R: A Language and Environment for Statistical Computing* (R Foundation for Statistical Computing, 2021).
79. M. I. Love, W. Huber, S. Anders, Moderated estimation of fold change and dispersion for RNA-seq data with DESeq2. *Genome Biol.* **15**, 550 (2014).
80. M. D. Robinson, D. J. McCarthy, G. K. Smyth, edgeR: A Bioconductor package for differential expression analysis of digital gene expression data. *Bioinformatics* **26**, 139–140 (2010).
81. M. E. Ritchie, B. Phipson, D. Wu, Y. Hu, C. W. Law, W. Shi, G. K. Smyth, limma powers differential expression analyses for RNA-sequencing and microarray studies. *Nucleic Acids Res.* **43**, e47 (2015).
82. L. Wang, Z. Feng, X. Wang, X. Wang, X. Zhang, DEGseq: An R package for identifying differentially expressed genes from RNA-seq data. *Bioinformatics* **26**, 136–138 (2010).
83. G. Yu, L.-G. Wang, Y. Han, Q.-Y., He, clusterProfiler: An R Package for comparing biological themes among gene clusters. *OMICS* **16**, 284–287 (2012).
84. S. Keleştemur, M. Altunbek, M. Culha, Influence of EDC/NHS coupling chemistry on stability and cytotoxicity of ZnO nanoparticles modified with proteins. *Appl. Surf. Sci.* **403**, 455–463 (2017).
85. K. Y. B. Lamm, M. L. Johnson, J. Baker Phillips, M. B. Muntifering, J. M. James, H. N. Jones, R. W. Redline, A. Rokas, L. J. Muglia, Inverted formin 2 regulates intracellular trafficking, placentation, and pregnancy outcome. *eLife* **7**, (2018).
86. E. C. Jensen, Quantitative analysis of histological staining and fluorescence using ImageJ. *Anat Rec (Hoboken)* **296**, 378–381 (2013).

Acknowledgments: We thank all the donors who participated in this study and the assistant from clinicians of The University of Hong Kong–Shenzhen Hospital. We are also grateful to the staff at the Faculty Core Facility, The University of Hong Kong, for technical assistance in this study. **Funding:** This work was financially supported by Hong Kong Research Grant Council grants (17112822 and 17115320), the High Level-Hospital Program, Health Commission of Guangdong Province, China (HKUSZH201902015), the HKU-SZH Fund for Shenzhen Key Medical Discipline (SZXK2020089). **Author contributions:** Conceptualization: P.C.N.C., Y.G., and Y.Y. Methodology: C.-L.L., T.Y., J.L., Z.Liu., X.L., Y.G., Y.Y., Y.-G.D., A.S.Y.K., K.-W.C., A.S.L.M., V.W.Y.N., L.Z., and M.C. Investigation: Q. Zhang, Q. Zeng, H.Z., X.F., and D.R. Visualization: Q. Zhang, Z.Li., and J.L. Supervision: P.C.N.C., Y.G., and Y.Y. Writing (original draft): P.C.N.C., Q. Zhang, and C.-L.L. Writing (review and editing): R.H.W.L., P.L., M.D., E.H.Y.N., Y.Y., P.C.N.C., and W.S.B.Y. **Competing interests:** A patent application related to the data presented here has been filed on behalf of The University of Hong Kong–Shenzhen Hospital (patent no. 2023110814626; issue date: 25 August 2023; current status: active; applicant: The University of Hong Kong–Shenzhen Hospital). The authors declare that they have no other competing interests. **Data and materials availability:** All data needed to evaluate the conclusions in the paper are present in the paper and/or the Supplementary Materials. All bioinformatic analyses were performed using publicly available software as described in Materials and Methods. Reagents, resources, and materials used in this study are detailed in table S2. The mRNA-seq data were deposited in the NCBI GEO database (www.ncbi.nlm.nih.gov/geo/) under the accession code GSE236475. The data that support the spatial-seq of villi have been deposited into CNGB Sequence Archive (CNSA) of the China National GeneBank DataBase (CNGBdb) with accession number STT0000042.

Submitted 28 April 2023
Accepted 3 October 2023
Published 3 November 2023
10.1126/sciadv.adi4777